FACTORS AFFECTING ROTOR STALL COMPUTATION BY COMPREHENSIVE ROTOR CODES

Berend G. van der Wall, German Aerospace Center (DLR), Braunschweig, Germany

Abstract

Comprehensive codes are the working horse for simulation purposes of a helicopter and its rotor under steady and unsteady conditions and they are also used to predict the operational limits until rotor stall. These limits are always dictated by aerodynamics – mainly flow separation due to airfoil stall – if not reached by other limits before. Accurate prediction of airfoil stall on rotating blades is a major challenge for comprehensive codes, despite many efforts spent on unsteady airfoil models. This paper focuses on hovering and high-speed rotor stall limits and on the factors that affect the rotor limits prediction.

1. NOTATION

Symbols

B	Effective non-dimens. blade radius
c	Blade chord, m
C_D	Helicopter drag coefficient
C_l, C_d, C_m	Aerod. lift, drag and moment coeff.
C_n, C_x	Aerod. coefficients normal to and in chord direction
C_Z, C_X, C_M	Leiss' airfoil coefficients
C_T, C_P	Thrust and power coefficient
FM	Rotor figure of merit
k	Reduced frequency
M, M_h	Mach number, hover tip Mach number
N_b	Number of blades
P_i	Induced power, kW
r	Nondimensional radial coordinate
r_{tl}	Non-dimensional tip loss radius
R	Rotor radius, m
Re	Reynolds number
y	Radial coordiante, m
α, α_{ss}	Aerod. and stall angle of attack, deg
β	Yaw angle, deg
β_p	Precone angle, deg
Θ_{tw}	Pretwist angle per radius, deg
Θ_{75}	Collective control angle, deg
Λ	Rotor disk aspect ratio
μ	Advance ratio
λ_i	Induced inflow ratio
σ	Rotor solidity
ψ	Rotor azimuth, deg
Ω, Ω_{TR}	Main, tail rotor speed of rotation, rad/s

Acronyms:

BVI	Blade-vortex interaction
CF	Centrifugal force
PW	Prescribed wake

2. INTRODUCTION

Since the end of the 1920s, when autogyros as first rotating-wing aircraft entered service, and 10 years later the helicopters, the trimmed maximum thrust capability of their main rotor was of interest. It defines the aerodynamic limit of the operational envelope from hover (helicopters only) or minimum speed (autogyros) to their maximum speed and maximum ceiling height. In those times the blade rotational speed of both types of rotating-wing aircraft was rather low with a blade tip Mach number around 0.4. Therefore, the envelope of rotor operation was essentially limited by stall and reversed flow conditions on the blades and not yet by compressibility effects on the advancing side.

Bailey, Gustafson and Myers at NACA experimentally investigated rotor blade stall on a YG-1B autogyro by observation of tufts attached to the blade surface, Refs. 1, 2. In Germany, Sissingh extended rotor aerodynamic theory by inclusion of steady airfoil stall, yawed flow effect on airfoil characteristics, and compressibility effects, Ref. 3. In helicopter developments at Focke and Flettner companies, compressibility effects were known to become important for future high-speed rotorcraft, highlighted by Focke, Ref. 4. German knowledge on rotorcraft theory and experiments was summarized after the second world war in Ref. 5.

By the end of the 1960s the rotor blade tip Mach number of helicopters increased to values around 0.65, balancing retreating blade stall and advancing blade compressibility effects for optimum helicopter performances throughout the flight regime. The centrifugal forces and the dynamic pressure (and with it the rotor thrust capability) acting on the rotor blades therefore rose twofold, the power required threefold.

In the early 1970s the rotor limits were explored numerically and experimentally, mainly at high speed and with focus on retreating blade stall. Bellinger (Ref. 6) found in comparison of theory with full-scale measurements of a H-34 rotor, that modeling unsteady airfoil characteristics is significantly improving the rotor lift prediction, yet not sufficient. Variable inflow and blade flexibility in flap and lag appeared unimportant, but elastic torsion was found to play a primary role, as it directly affected the angle of attack.

The effect of Reynolds number on rotor stall was investigated by Hardy (Ref. 7) on 2D data for the Vertol 23010-1.58 airfoil. A large influence on maximum lift coefficient was found at low Mach numbers. Up to Mach numbers of 0.6 this effect diminished. For an advance ratio of 0.3, rotor measurements were made with a fixed collective and zero cyclic control angles, but the shaft angle varied from -35 deg towards zero, with progressive stall developing and reducing the rotor lift curve slope.

McCroskey (Ref. 8) performed $1{:}7.5$ model-scale experiments with a CH-47C rotor with a pressure sensor instrumented section at 75 % radius. In hover measurements, the rotating blade stall was still showing the leading-edge pressure peak while in the 2D data the peak collapsed. This results in higher maximum lift coefficients in the rotating case. In forward flight with an advance ratio of $\mu = 0.35$, rotor stall was investigated with a fixed collective control angle and varying the shaft angle of attack as in Ref. 7, thus no trim was performed on the rotor and only stall characteristics were studied.

Landgrebe and Bellinger (Ref. 9) performed a study on model rotor stall with eight variations of twist, airfoil, taper, number of blades and torsional frequency, while keeping radius, chord, tip Mach number and hinge offset constant. Because of a very low tip Mach number below 0.3 only minor compressibility effects were observed. Again, no cyclic control angle was used to trim the rotor.

Amer and LaForge (Ref. 10) showed that the maximum thrust capability of teetering and articulated rotors is the same in the range of advance ratios $\mu =$ 0.25 to 0.36, based on steady-state trimmed flight test data at the never-exceed velocity for different flight levels. They are also equal during pull-up maneuvers, shown for advance ratios ranging from $\mu = 0.15$ to 0.39, but these are transient values.

McHugh (Ref. 11) examined the lift limits of a $1{:}10$ model-scale CH-47B/C rotor, based on wind tunnel tests of from hover up to advance ratios of $\mu = 0.64$. The rotor was trimmed to lift and propulsive force and to minimum flapping using collective and cyclic control angles and the shaft angle. As a result, the maximum trimmed rotor lift limits could be evaluated, which depended on the propulsive force $C_D/(\Lambda\sigma)$ required, see Figure 1.

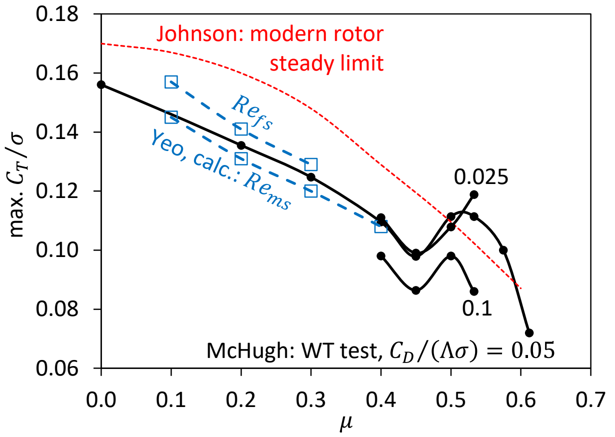

Figure 1: McHugh's maximum rotor lift limits curve, $1{:}10$ scale CH47B/C rotor, 620 ft/s tip speed, with Yeo's calculations (Ref. 12) of model- and full-scale Reynolds numbers and Johnson's level flight limits of modern rotors (Ref. 14).

The rotor disk aspect ratio is $\Lambda = 4/\pi$ and C_D is the helicopter drag coefficient. Much later, Yeo (Ref. 12) calculated these limits using CAMRAD II, Ref. 13, to predict the rotor performance and loads. His results for model-scale Reynolds numbers Re_{ms} come close, but do not reach the model-scale test data. Full-scale computations (Re_{fs}) with higher maximum lift coefficients of the same airfoil are above the model-scale data. In addition, Johnson (Ref. 14) sketched the lift limits of modern rotors (with advanced airfoils and modern blade planforms) in level flight. With increasing flight speed the maximum lift capability reduces due to the increasing asymmetry of dynamic pressure on advancing and retreating side, which limits the capability of trimming the rotor.

The availability of computers enabled engineers to develop comprehensive simulation codes (e.g. CAMRAD II, Ref. 13) for a fast evaluation of helicopter and rotor performance, including dynamics, aerodynamics, and the rotor wake with an ever-increasing variety of models and refinements, representing the physics in an engineering manner.

In pre-design studies and real-time helicopter simulations the simplicity of these models is essential, yet these have to represent the main features reliably well and physically correct. For the aerodynamics, often table look-up methods are used, including steady stall and compressibility of the airfoils used, but lacking unsteady aerodynamics such as dynamic stall with stall delay and post-stall vortex shedding. Also, yawed flow causes an advantageous stall delay, as do centrifugal forces in the boundary layer especially at the inboard regions of a rotor blade.

When reaching the rotor lift limits, the ability to model dynamic stall in combined unsteady yaw and periodic free-stream velocity becomes increasingly important to predict the maximum rotor lifting capabilities, which has been demonstrated in a dynamic stall GARTEUR activity, Ref. 15. Measurements on a model rotor with reduced tip speed at an advance ratio of $\mu = 0.4$ were used to validate and improve comprehensive code prediction capabilities. The rotor was trimmed to the values measured in the wind tunnel: shaft angle, rotor lift, propulsive and lateral forces. With increasing lift, deep stall was encountered. The simulations using comprehensive rotor codes were only able to compute the highest rotor lift (if at all), when both dynamic stall and yawed flow models were enabled.

Besides the blade pretwist distribution and its pitch angle (due to pilot controls and elastic torsion), the induced inflow model used is also essential for the local aerodynamic angle of attack, and thus the stall onset at large thrust. A variety of models exist based on momentum theory (constant, or with longitudinal and/or lateral gradients), potential theory, and vortex theory (with prescribed or free-wake geometry).

The loss of lift due to flow around the blade tip is often treated by simply cutting off the two-dimensional lift distribution at an “effective” non-dimensional radial station B (the equivalent at the blade root usually is neglected). This simultaneously increases the mean induced inflow ratio because of the reduced effective rotor disk area. Such a crude approximation is not representing the actual cause of the lift dropping to zero at the blade’s end, namely, the induced velocities. Therefore, a more physical approach should be used, such as the Prandtl/Betz formulation in Ref. 16, or a simpler approximation to it.

Since all these factors impact the capability of comprehensive codes to predict rotor stall and trimmable rotor thrust limits in hover and forward flight, their impact and importance is investigated in this paper. In order to isolate aerodynamics issues from blade design parameters (e.g. geometry, taper, twist, sweep, an-/dihedral, elasticity, airfoil selection), the blade is treated as stiff, based on the Bo105 Mach-scaled model rotor geometry. Other limits – most often reached before the aerodynamic rotor limits – such as: structural load limits, maximum available power, or mechanical limits of blade pitch control, are ignored in this study to focus on the pure aerodynamic limits that are the boundary of a trimmable rotor with maximum possible thrust.

3. SEMI-EMPIRICAL PHYSICAL MODELS

3.1. Rotor blade model

As example rotor, the Bo105 Mach-scaled model rotor with rectangular blades is used. Its characteristics are given in Table 1.

Table 1: Mach-scale model rotor characteristics.

Characteristic	Symbol	Metric
Radius	R	2.0 m
Chord length	c	0.121 m
Aerodynamic root cutout	y_a	0.44 m
Radius of zero twist	y_{tw}	1.5 m
Number of blades	N_b	4
Precone	β_p	2.5 deg
Pretwist per radius	Θ_{tw}	-8 deg
Airfoil, tabbed trailing edge	NACA	23012
Speed of rotation	Ω	109 rad/s
Tip speed	ΩR	218 m/s
Hover tip Mach number	M_h	0.639
Solidity	σ	0.077
Nominal thrust coefficient	C_T	0.00547
Nominal blade loading	C_T/σ	0.071

Radius and root cutout are scaled to 40.73 % of the full-scale vehicle, while the chord length is scaled to 44.81 % to partly account for loss of maximum lift capability due to lower Reynolds numbers of the model rotor. Thus, the resulting solidity σ is $10\,\%$ larger than that of the full-scale rotor. The tip Mach number is the same as the full-scale rotor. The nominal thrust coefficient is based on a 2.46-ton Bo105 as starting value for a thrust sweep towards the maximum trimmable limit.

DLR's high resolution rotor simulation code S4 is used, a detailed description of its features is given in Ref. 17. Within the simulation the rotor blade is represented by 20 elements of equal annulus surface in the rotor disk, leading to wider elements at the root (where low dynamic pressure is present) and progressively smaller ones towards the blade tip (with the highest dynamic pressure and where the largest radial gradients of lift are to be expected), as shown in Figure 2. The dashed line marks the pitch axis at quarter-chord and the $+$ symbols denote the points at three-quarter chord, where the velocities acting normal and tangential to the chord line are computed, including the pitch rate (due to blade pitch control) times semi-chord.

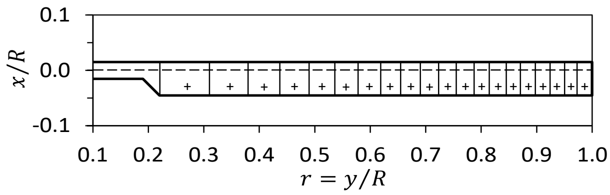

Figure 2: Model rotor, 20 blade element distribution

3.2. Airfoil model

The classical way to compute section lift, drag and moment coefficient in comprehensive codes is based on steady table look-up method. With the local Mach number and angle of attack, both computed by the velocity components acting on the section of interest, the coefficients are interpolated from the table. Although these include compressibility and steady stall effects, they usually do not include yaw effects or dynamic stall, because that would require multi-dimensional tables. The inclusion of yaw angle and centrifugal force effects on the steady stall angle of attack α_{ss} and the representation of dynamic stall hysteresis including lift overshoot calls for an analytical formulation of the airfoil coefficients instead of table look-up methods.

In the 1970s several unsteady aerodynamic methods, partly based on the tables with addition of unsteady contributions, partly fully analytical computation of the coefficients, have been developed, e.g. by Gormont (Ref. 18), Bielawa (Ref. 19), Tran (Ref. 20), Beddoes (Ref. 21), Gangwani (Ref. 22), Leiss (Refs. 23, 24), Leishman (Ref. 25), Petot (Ref. 26), and Truong (Ref. 27).

Here, the Leiss model (Refs. 23, 24), applied to the Bo105 NACA 23012 airfoil (Ref. 28), is used. It has been applied to other airfoils and validated, for example, in Refs. 15, 17. Airfoil coefficients of this model are acting at the quarter-chord point normal to the chord line ($C_Z = C_n M^2$, positive up), in chordwise direction ($C_X = C_t M^2$, positive forward) and the moment about the quarter-chord point ($C_M = C_m M^2$, positive nose-up). They are based on the sonic speed dynamic pressure and, hence, they directly represent non-dimensional forces and moments. The conversion of these coefficients is shown in Figure 3.

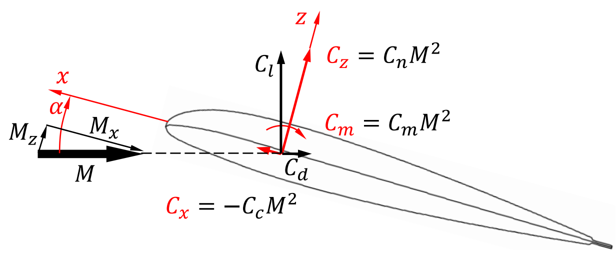

Figure 3: Conversion of aerodynamic coefficients

The fully analytical semi-empirical formulation includes compressibility effects and stall, and covers the entire range of angles of attack from $\alpha = -180$ deg to $+180$ deg in purely analytical form. Reversed flow, however, usually is confined to Mach numbers of $M_h(\mu - r_a)$ at $\psi = 270$ deg azimuth on the retreating side, which for this rotor in maximum reaches a value of $M = 0.179$ for a high advance ratio of $\mu = 0.5$. In this case, the advancing tip at $\psi = 90$ deg azimuth experiences already a Mach number of 0.959.

The steady stall angle of attack depends on the Mach number M, and is large in incompressible flow, while in the higher subsonic speed range it progressively approaches much smaller values. At nominal rotational speed of the rotor the variation of steady stall angle is given in Figure 4. The circles denote the position of blade element collocation points. The Mach number here also is a direct measure of the blade radial coordinate y or r, as it grows linearly with it.

In rotating wing experiments it was found that especially inboard near the hub the centrifugal force (CF) acting on the boundary layer generates significantly higher maximum lift coefficients, compared to 2D flow conditions. This effect progressively dies out towards the blade tip and can be interpreted as a shift of the steady stall angle of attack to higher values. In this study that effect is simulated empirically by an offset $\Delta\alpha_{ss,CF}(r) \propto 1/r$ with the offset at the blade root $r_a = y_a/R$ as sole characteristic parameter. In this study, an empirical value of $\Delta\alpha_{ss,CF}(r_a) = 4$ deg is used.

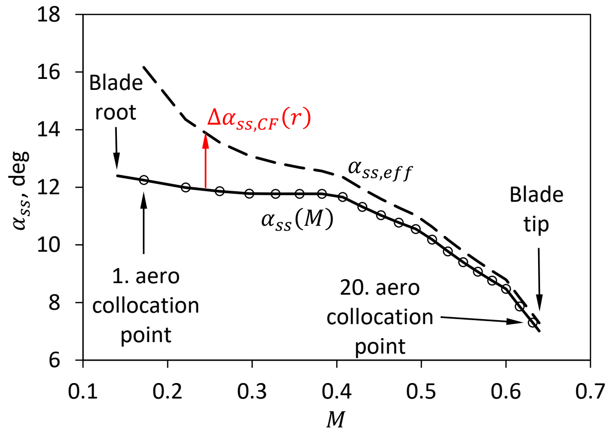

Figure 4: Steady stall angle of attack in hover, without (solid) and with inclusion of centrifugal force (CF) effect (dashed).

For large radii this stall offset approaches zero and then represents the 2D airfoil characteristics. It is understood that this is a crude approximation and requires reliable data for a better representation of the physics, but at least it is a physically meaningful approach to study the impact of such an effect on rotor stall. In application, this offset is used the same way as if it was caused by a yaw angle, also delaying the stall angle of attack.

The conversion of the Leiss' coefficients to the classical lift, drag and moment coefficients based on the dynamic pressure of the velocity components is shown in Figure 3 and given by Eq. (1). The trigonometric functions can be replaced by the Mach components acting in chordwise direction, M_x, and normal to it, M_z: $\cos\alpha = M_x/M$ and $\sin\alpha = M_z/M$

(1)
$$
\begin{aligned}
C_l &= \left(C_Z \cos\alpha + C_X \sin\alpha\right) / M^2 \\
C_d &= \left(C_Z \sin\alpha - C_X \cos\alpha\right) / M^2 \\
C_m &= C_M / M^2
\end{aligned}
$$

An example for lift, drag and moment coefficients is given in Figure 5, where the black line represents the 2D steady airfoil characteristics without CF effect and the red line with inclusion of it, for two radial stations (one inboard and the other outboard) and their respective Mach numbers. The upper graph shows data for the first blade element with $r = 0.269, M = 0.172$, i.e. incompressible flow, and the lower graph data for $r = 0.964, M = 0.618$ in the compressible range near the blade tip. The example is computed using the rotor at nominal speed of rotation, $\mu = 0$, without downwash and tip loss, steady aerodynamics, without and with the CF model. The range of angles of attack is obtained by a collective control angle of 6 deg (without CF) or 10 deg (with CF) to include the stall angle in either case, and 10 deg cyclic control is applied to cover a sufficient range of angle of attack.

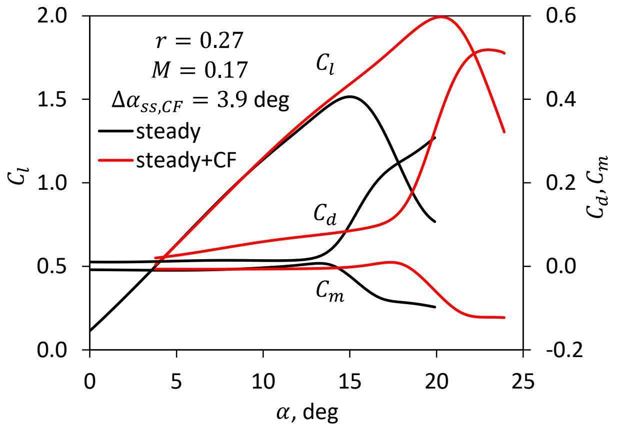

(a) incompressible flow regime near the root

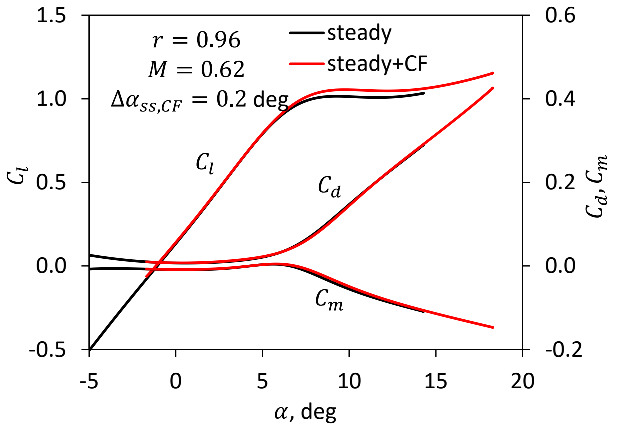

(b) compressible flow regime near the tip

Figure 5: Steady airfoil characteristics in hover, without (black) and with inclusion of centrifugal force (CF) effect (red).

Even in steady post-stall conditions the aerodynamic coefficients show unsteady behavior with stochastic variations of frequency and magnitude, due to permanent vortex shedding. Although a model for such post-stall vortex shedding (VS) was developed in the 1990s, Ref. 15, a reduced form is used here. It includes a fixed frequency depending on Mach number and a magnitude of constant value in deep stall, which diminishes when approaching the stall angle of attack. This is shown exemplarily in Figure 6, where for a radial station of $r = 0.598$ a constant Mach number of 0.38 is present. The computational setup is as before, without CF effect, but with a collective control angle of 10 deg and 15 deg cyclic control applied to cover a range far enough above the stall angle. The thick black line represents the airfoil data without VS, the thin line with VS added.

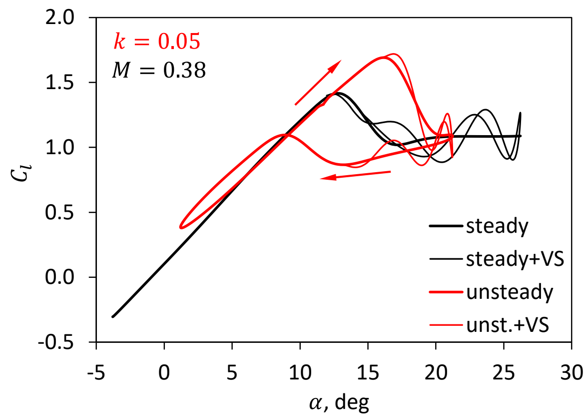

(a) lift coefficient

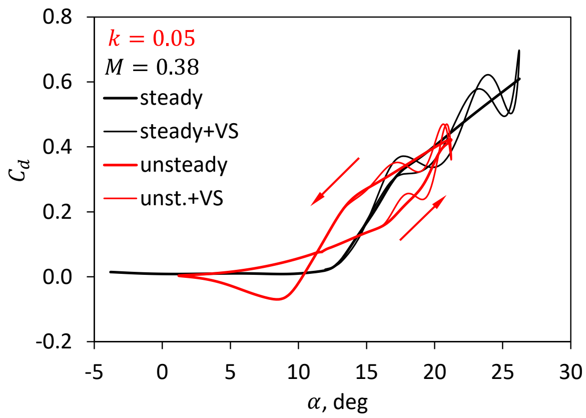

(b) drag coefficient

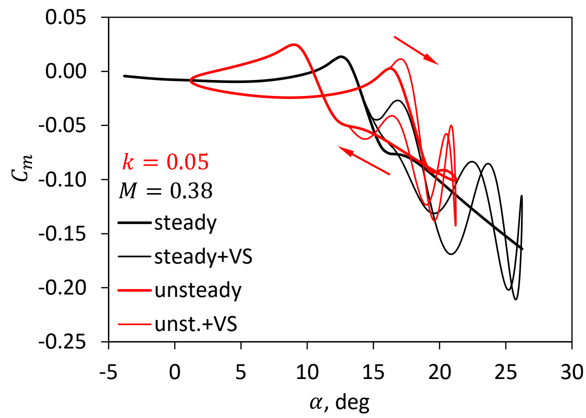

(c) moment coefficient

Figure 6: Steady (black) and unsteady (red) airfoil characteristics in hover, without and with inclusion of vortex shedding (VS) effect.

Because this application with a cyclic control angle is an unsteady motion, the unsteady aerodynamics model needs to be switched on, which adds three effects: first, a phase delay of the effective angle of attack relative to the geometric incidence angle as described by the Theodorsen function (Ref. 29), second, a stall onset delay and that of re-attachment, third, apparent masses (non-circulatory forces and moments).

The phase delay results into a hysteresis, the stall delay causes a significant lift overshoot in the upstroke motion and a significant delay of flow re-attachment during the downstroke. All this is shown by the red curves in Figure 6, where the mean angle is the same as for the steady data, but the amplitude of the cyclic control angle is reduced to 10 deg. In addition, the thin red line indicates the additional dynamics when the VS model is switched on.

A validation of the model with experimental steady and unsteady data of an OA213 airfoil in 2D flow and with $\beta = 22$ deg yawed flow condition at a Mach number of 0.18 was performed within a GARTEUR activity, Ref. 15.

Steady measurements were performed first with time-averaged results, thus no vortex shedding in the stalled region could be seen. The airfoil was periodically pitched at a reduced frequency of $k = (\omega c)/(2V) = 0.05$ and data for several individual successive cycles were made available. The VS model included random variations of frequency and magnitude in the GARTEUR study, such that each cycle is different, as is in the experiment. Lift and moment coefficients are compared to the model in Figure 7.

The model is correctly predicting the steady as well as the unsteady lift coefficient loops, also the difference between unyawed and yawed conditions, all included in Figure 7 (a) for better direct comparison. The latter exhibits a smaller lift curve slope, a thinner dynamic stall hysteresis and a little higher maximum lift coefficient at a significant higher stall angle of attack, both in the steady and unsteady cases.

The aerodynamic moment shown in Figure 7 (b) for the unyawed case and in Figure 7 (c) for the yawed condition also reveal that the model is correctly predicting the change of the steady and dynamic airfoil characteristics. As in the case of the lift coefficient, the yaw angle shifts the moment stall (steady and unsteady) to larger angles of attack.

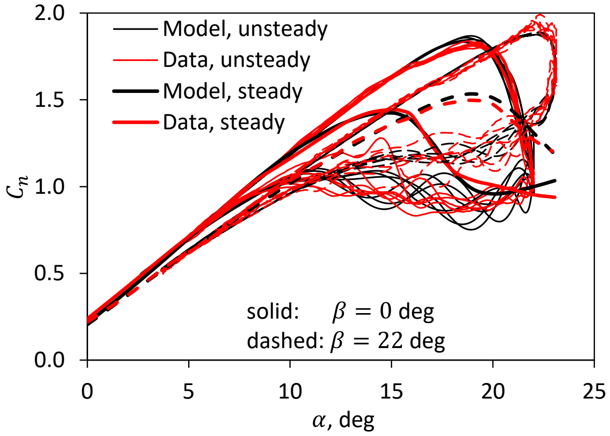

(a) normal force coefficient, yawed and unyawed

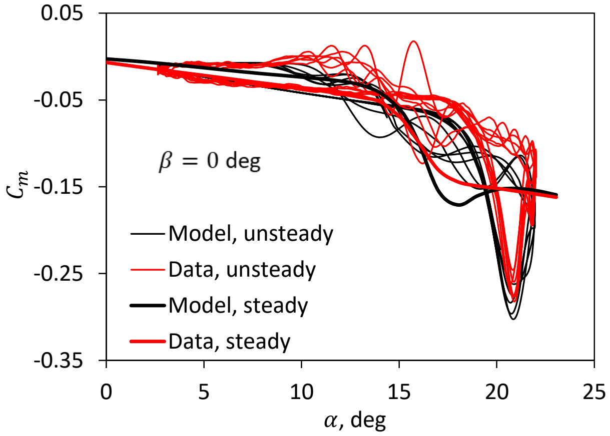

(b) moment coefficient, unyawed

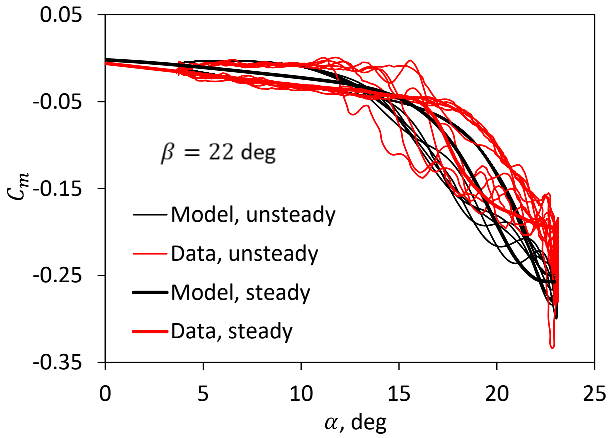

(c) moment coefficient, yawed

Figure 7: Validation of the unyawed and yawed, steady (time averaged) and unsteady (with vortex shedding), attached flow and dynamic stall aerodynamic model with data of the OA213 airfoil (from Ref. 15).

Drag data were not available, thus they cannot be compared here with experimental data.

3.3. Inflow models

Inflow models investigated are: no inflow ("None"), constant inflow (here called the "Glauert" model from momentum theory, Ref. 30), inflow including linear longitudinal and lateral variation (here called the "Drees" model, Ref. 31), a potential theory based model with nonlinear radial and multi-harmonic circumferential distribution (the "Mangler" model, Ref. 34), and a vortex wake method with computationally efficient prescribed geometry (called prescribed wake, "PW", as used by DLR e.g. in Ref. 17).

In hover, Glauert and Drees are identical, just the Mangler model has a nonlinear radial variation of induced velocities, but is constant in circumference. In forward flight, the Drees model has a longitudinal and lateral gradient relative to the same mean values as of Glauert. The Mangler model is laterally symmetric, which leads to a non-linear longitudinal gradient and results in radially nonlinear distributions with multi-harmonic periodic variation in circumference of the rotor disk.

The prescribed wake (PW) model generates nonlinear inflow distributions all over the disk. It is fed by trailed vorticity all along the span within the near wake. Up to three trailed vortices are kept in the far wake: one at the root, one at the tip and – depending on the lift distribution near the tip – a secondary more inboard tip vortex of opposite sense of rotation.

The wake contraction is prescribed and its geometry is based originally on Beddoes' model (Ref. 35), and later on was significantly enhanced to include both the root cutout region and the harmonic loading effects on the wake geometry perturbations, Ref. 36, as well as the perturbations due to the presence of a fuselage, Ref. 37. An example radial distribution of induced inflow ratio in hover for all these models is shown in Figure 8.

The Mangler model represents a distribution similar to an expected lift distribution, while the PW distribution of induced inflow up to 80 % radius is more parallel to the constant inflow and near the tip reducing, due to the wake contraction and the upwash generated by the tip vortices of the preceding blades. The mean value, however, is the same for all.

3.4. Tip loss model

The simple, but non-physical cutting off the blade tip at a non-dimensional effective radius B is often used (mostly selected as $B = 0.97$).

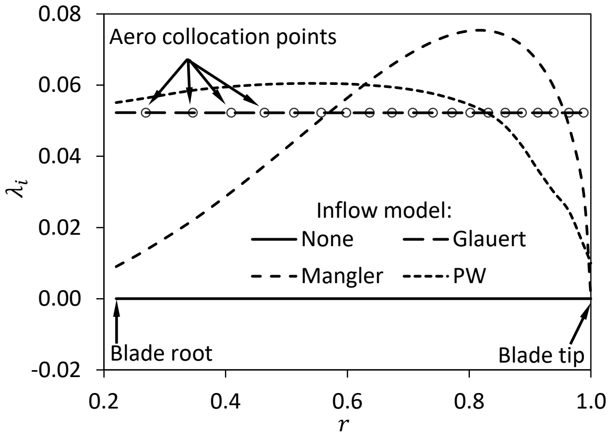

Figure 8: Example distributions of induced inflow ratio from various models in hover, $C_T/\sigma = 0.071$.

It can be computed based on the thrust coefficient as $B = 1 - \sqrt{2C_T}/N_b$, a result suggested by Prandtl (Ref. 16). Wheatley (Ref. 32) suggested a tip loss factor independent of thrust, just based on the blade geometry: $B = 1 - c/(2R)$, and similarly Sissingh (Refs. 3, 33) by $B = 1 - c/(1.5R)$. The blade element aerodynamics are treated as purely 2D from the blade root to the effective radius B, and the momentum-based induced velocity is corrected due to the reduced rotor disk area by $\lambda_{i,eff} = \lambda_i/B$. Example values for B using the different methods are given in Table 2. With increasing thrust, Prandtl's method leads to smaller B, which appears more physical due to increased tip vortex strength and increased radial portions affected by it. However, for nominal thrust and twice of it, the values computed by the other methods are rather close to Prandtl's result.

Table 2: Examples for effective radius B, rotor data from Table 1.

C_T	C_T/σ	Prandtl	Wheatley	Sissingh
0.0	0.0	1.000	0.97	0.96
0.00547	0.071	0.974	0.97	0.96
0.01094	0.142	0.962	0.97	0.96
0.01641	0.213	0.954	0.97	0.96

In the S4 code the tip losses are introduced in a semi-empirical manner by additional induced velocities, as if generated by a continuous trailed vorticity, and the root losses are also accounted for in this manner. This allows to combine any inflow model with more realistic lift losses in the tip and root region. The additional induced velocities begin with zero at a radial station r_{tl} indicating the begin of the tip loss region, and progressively increase until at the blade tip itself the zero-lift angle of attack is obtained, leading to zero lift there, as required, which approximates the Prandtl-Betz tip loss formulation (Ref. 16). The innermost element of the blade is treated the same way.

This tip loss parameter r_{tl} is varied in the range $0.8, 0.9, 0.95$ and 1.0 (which means: no tip loss) to study its effect on the results. Considering a constant 2D lift coefficient of unity, the tip loss model leads to a continuous progressive drop towards zero in the tip and root region as shown in Figure 9 (a). The actual lift force distribution is based on the local dynamic pressure, i.e. proportional to $r^2 C_l$, and sketched in (b).

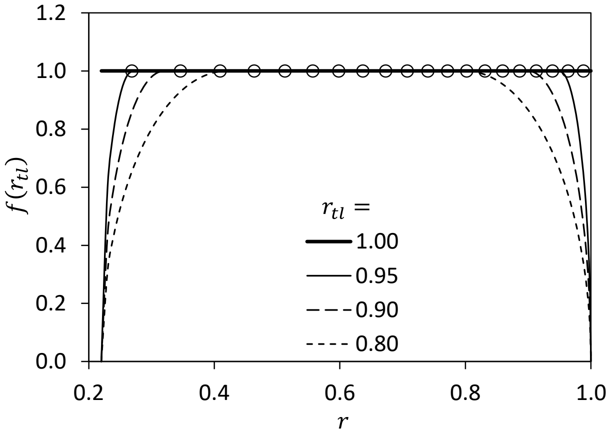

(a) 2D lift coefficient of unity

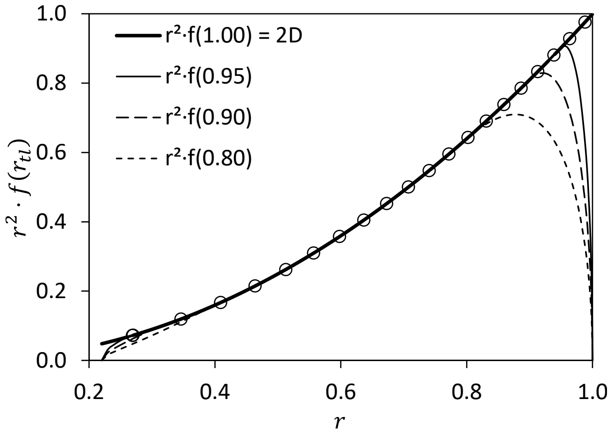

(b) 2D nondimensional lift, based on (a)

Figure 9: Root and tip loss impact on lift distribution for various r_{tl} values.

It appears justified to ignore the small overall loss at the root region, compared to that at the blade tip. It is interesting which value of r_{tl} is approximately representing an equivalent to the loss caused by cutting off the blade at the typical value of $B = 0.97$. This is shown in Figure 10, where only the tip region of Figure 9 (b) is shown. The area shaded in red is the loss due to cutting off at B. It appears rather equivalent to selecting $r_{tl} = 0.9$, generating the loss of the area shaded in blue, which appears little less than the red one. $r_{tl} = 0.8$ will be more equivalent to a factor of $B = 0.96$.

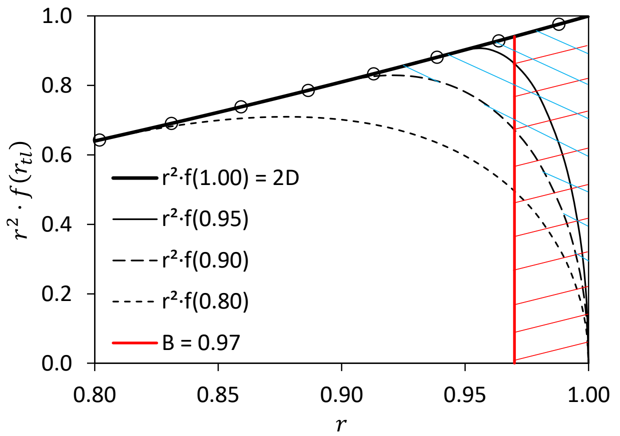

Figure 10: Comparison of tip loss methods in the tip region of Figure 9 for various r_{tl} values from 0.8 to 1.

4. RESULTS

In general, the following procedure is applied: a trim is performed with prescribed shaft angle and zero rotor hub rolling and pitching moments. It starts with blade loading of nominal thrust ($C_T/\sigma = 0.071$) and is first increased in constant increments. When stall is encountered, the increment is reduced to progressively finer steps until the maximum trimmable thrust is reached and the rotor lift curve slope with respect to the collective control angle becomes zero: $dC_T/d\Theta_{75} = 0$. This procedure is repeated for a range of parameter variations of the different aerodynamics models described in the section before, as there are:

- Airfoil aerodynamics: steady / unsteady
- Yaw (including CF) model: off / on
- VS model: off / on
- Inflow model: None / Glauert / Drees / Mangler / PW
- Begin of tip loss: $r_{tl} = 0.8$ / 0.9 / 0.95 / 1.0

In order to reduce the theoretical number of combinations of all these, the VS and yaw models were individually applied only to the $r_{tl} = 0.9$ setting. The VS model introduces another difficulty, because the frequency of vortex shedding is modeled in dependence of the Mach number and therefore differs for each radial position, and it is in general no integer harmonic of the rotor rotational frequency. Therefore, each individual revolution is slightly different and no steady mean rotor thrust and hub moments can be obtained anymore. Then, sufficient thrust and hub moment thresholds must be allowed when trimming, such that the thrust fluctuations remain within the thresholds specified.

The trim computation is based on a single blade only, assuming all blades experience the same at the same azimuth, which ensures the periodicity. The trim accuracy was set very tight to 1 N in thrust and 1 Nm in hub moments. For a maximum thrust in hover of up to 11 kN this trim tolerance is less than 0.1 permille.

4.1. Hover: maximum thrust and figure of merit

General remarks

In hover, no cyclic control angles are needed due to constant circumferential flow conditions. Therefore, even the region above rotor stall can be explored by $1, 3, 5$ and 10 deg of collective settings above that of the individual maximum thrust. Such further increase of collective control angle reveals an initial loss of thrust due to increasing stall regions on the rotor blade. A further increase of Θ_{75} then again generates an increase of thrust, similar to the individual steady airfoil lift coefficient behavior when going far beyond stall. In hover, the Glauert and Drees inflow model generate the same result, a constant inflow all over the disk, thus only the Glauert model was applied.

As long as attached flow is present everywhere, constant circumferential flow condition is a valid assumption. When stall occurs, unsteady flow structures develop, for example due to VS. This does not only affect the blade element(s) generating it, but the vortical structures also are released to the flow and will possibly be encountered by the following blades. However, this will happen only at high thrust that comes along with a high induced velocity, transporting these disturbances downwards and away from the rotor. Therefore, here the assumption is made that such turbulence may be ignored and each blade is operating in a generally undisturbed free-stream, even when experiencing deep stall.

Consequently, the application of the unsteady aerodynamics model is no different to the steady model, but the VS model may be switched on to generate periodically oscillating aerodynamic coefficients of the blade elements operating in the post-stall regime.

Rotor thrust, power and figure of merit

Results for a thrust sweep (from its nominal value to 10 deg of collective control angle above that of the individual maximum thrust) with every combination of inflow model (None, Glauert, Mangler, PW) are given in Figure 10. In addition, $r_{tl} = 0.9$ is also combined with the centrifugal force model (CF). The blue dots are experimental data from the Bo105 model scale rotor obtained in the DNW, Ref. 38, that reach up to only $C_T/\sigma = 0.106$, within the attached flow regime.

In contrast to the assumptions made for the computations of this paper, the tested rotor blades were flexible, slightly dissimilar, and develop an increasing amount of steady elastic twist with rising thrust. The test was conducted in the open-jet closed test hall of the DNW-LLF. Therefore, air turbulence increased that was re-ingested into the rotor at high thrust, which caused increasing vibration and a further thrust increase was abandoned.

The absence of any inflow, as expected, leads to a steeper thrust increase than with any of the inflow models (with according offset of the collective control angle), and to the highest maximum thrust; the reasons will be shown later. Due to the absence of inflow, only profile power is developing because of airfoil drag, which in attached flow is relatively small, but significantly rises in stall. Because of the missing induced power, its figure of merit FM is above 1 for a wide thrust range. Only in deep stall regions the profile power becomes large enough to result in $FM < 1$.

The Glauert and prescribed wake (PW) inflow appear rather similar in their results, with a gradual decrease of thrust beyond its limit. The Mangler model reaches a maximum thrust between the Glauert and None inflow models, and with a sharper loss above the maximum thrust, similar to the curve of None inflow. In all cases, no tip loss $r_{tl} = 1.0$ allows for the highest maximum thrust. With r_{tl} moving inboard, maximum thrust is reduced continuously because of lift loss mainly at the blade tip, and to a much lesser degree also at the blade root.

Regarding the power prediction, all inflow model results appear rather similar to each other. The experimental thrust and power curves are matched by all three inflow methods, with best fit of the Mangler model. The effect of r_{tl} variation is in accordance with its impact on thrust. Any loss of lift at the tip is associated with a reduction mainly of the induced and also of the airfoil drag there, and due to the long arm to the rotor center it is reducing the power.

More sensitive to power prediction is the figure of merit FM. The best fit to the test data is seen for the Mangler model with a tip loss beginning between $r_{tl} = 0.8$ and 0.9. As expected, the highest possible FM is obtained without tip loss, $r_{tl} = 1.0$, and in the region around $C_T/\sigma = 0.11$, i.e., in the region of attached flow, but close to stall.

The figure of merit of the None inflow model reaches highest values at $C_T/\sigma = 0.14$ as high as $FM = 3.81$ for $r_{tl} = 0.8$ and even $FM = 5.38$ for $r_{tl} = 1.0$. In the absence of induced drag, except for the tip loss region, this result cannot be compared with the others and was only added for completeness.

The centrifugal force model (CF) was only applied to the $r_{tl} = 0.9$ setting and its results are given by the red lines. As long as the flow is attached, there appears no difference to the former cases without inclusion of the CF model. Once stall starts to develop, the CF model generates a delay of the steady stall angle of attack and an increase of the maximum lift coefficient to larger values, see Figure 5. This generates a higher maximum thrust capability, and also a higher thrust in the post-stall regime, while the power appears only slightly increased over the value without the CF model.

The same is seen in the impact of the CF model on the FM, independent of the inflow model used. In attached flow, the slight increase of power results in little lower FM than without the CF model and the higher maximum and post-stall thrust shifts the curves to the right.

The results for the maximum rotor thrust are summarized in Figure 12 (a). For each of the inflow models used, the reduction of the tip loss area increases the maximum trimmable thrust by about the same amount, and the same applies when adding the CF model. Its main parameter, the stall delay at the blade root, was kept constant here without further variation. The respective power required for the maximum thrust is shown in Figure 12 (b). It increases according to the thrust of the individual inflow model shown in (a), only the PW model results in a steeper increase of power than the other inflow models.

The None inflow model leads to a power about $1/3$ of that of the other inflow models, which represents the pure profile power in case of no tip loss ($r_{tl} = 1$). The power appears insensitive to the tip loss region, but this is misleading. Since $r_{tl} = 0.8$ leads to a significantly smaller maximum thrust, less power might have been expected because of lower airfoil drag due to smaller angles of attack. But, because the tip loss is modeled by induced velocities, the tip region now introduces additional induced power, that widely compensates for the reduced drag power.

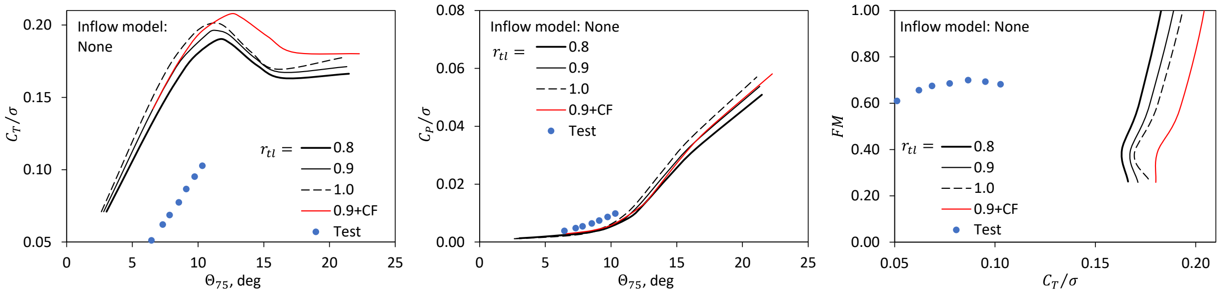

(a) No inflow (None)

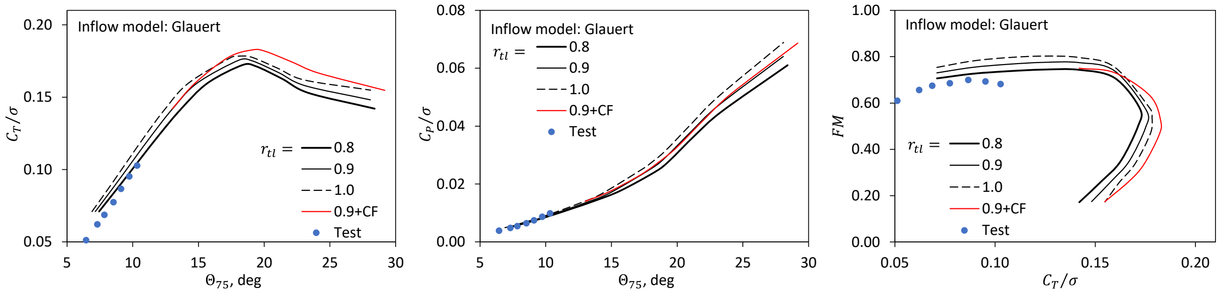

(b) Constant inflow (Glauert)

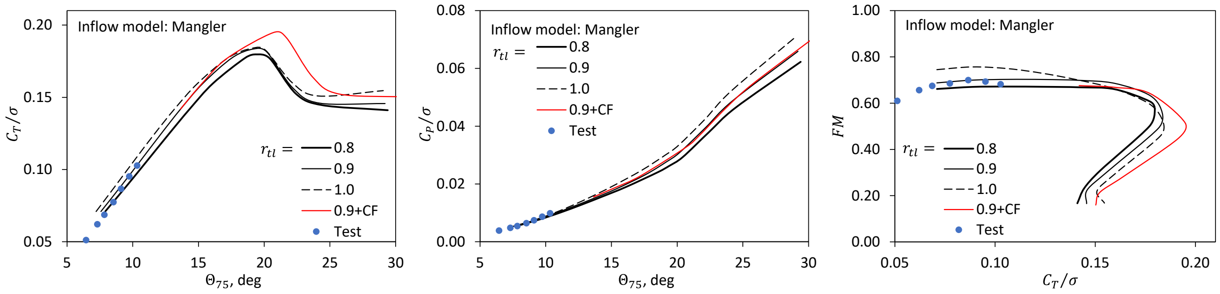

(c) Nonlinear inflow (Mangler)

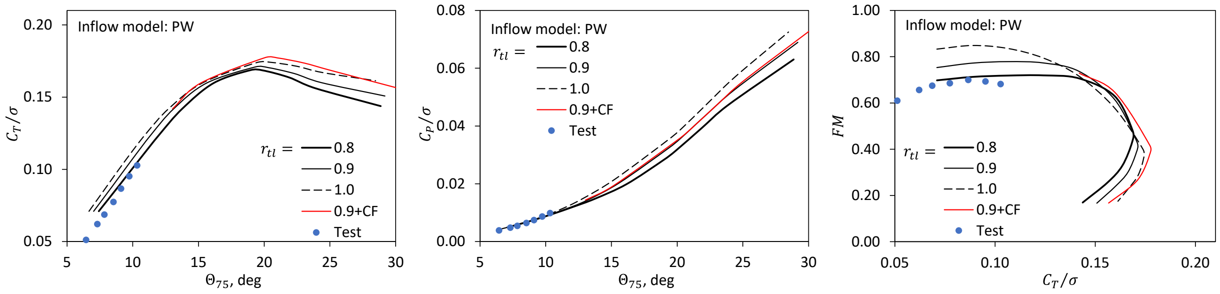

(d) Prescribed wake (PW)

Figure 11: Influence of the inflow model, the tip loss parameter r_{tl} and centrifugal force CF model on thrust (left), power (middle) and figure of merit (right).

The CF model increases the power required at maximum thrust in all cases, in agreement with the increase of the maximum thrust itself. It is also observed in Figure 12 that the power level is depending on the inflow model used. Although the PW inflow reaches the lowest maximum thrust, its power is the highest. The Mangler inflow model predicts higher thrust, but also requires more power than the Glauert inflow.

In order to understand this, the radial distribution of the inflow ratio λ_i needs to be investigated. In Figure 13 it is given for the nominal thrust ($C_T/\sigma = 0.071$, black curves), a rather high thrust commonly achieved by all inflow models ($C_T/\sigma = 0.16$, red curves), at a condition 5 deg in collective control angle larger than that of the maximum thrust. The latter is different for each inflow model (C_T/σ differs, blue curves), but in every case represents a deep stall condition for the rotor. The tip loss factor is set to $r_{tl} = 0.9$ in every case and the different inflow models used are identified by different line styles.

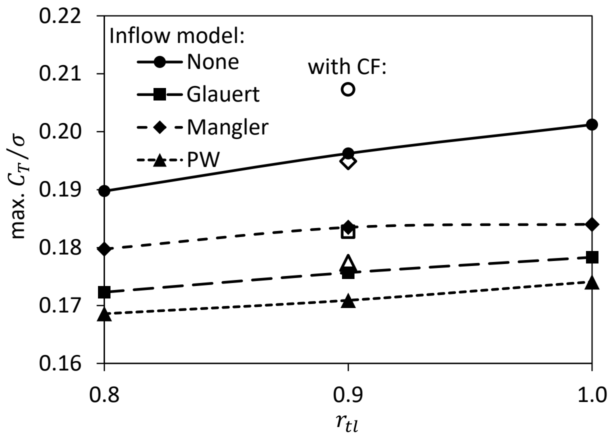

(a) maximum trimmable thrust

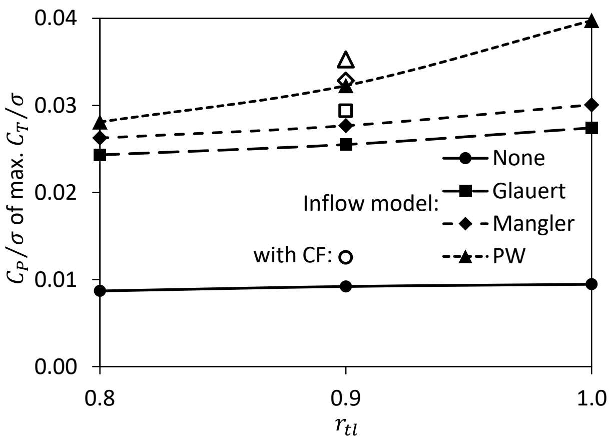

(b) power required at maximum trimmable thrust

Figure 12: Influence of tip loss, inflow and CF models on maximum rotor thrust and power required.

Because of the tip loss beginning at $r_{tl} = 0.9$, also the "None" inflow model includes induced inflow progressively increasing towards the tip and the root of the blade, which is in effect for all other inflow models, too; compare to $r_{tl} = 1.0$ (= 2D from root to tip) as shown in Figure 8. Outboard of $r \approx 0.65$ the Mangler model generates the highest induced inflow and the PW model the lowest, which is due to the tip vortex quickly moving inboard and then inducing an upwash at the outer region $0.85 < r < 1$. Inboard of $r \approx 0.65$ the PW generates the highest inflow and the Mangler model the lowest.

The section angle of attack α can be computed based on the collective control angle required for the respective thrust, the circumferential velocity, and the inflow. It is shown in Figure 14 for the same conditions as in Figure 13, together with the stall onset boundary (see Figure 4). Because of the smaller circumferential velocities at the inner radial stations the same inflow ratio leads to larger angles of attack there than at the outer radial stations.

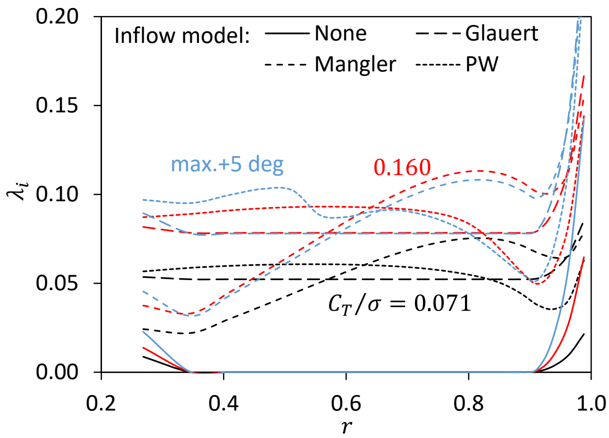

Figure 13: Radial distributions of the inflow ratio for various thrust levels and inflow models in hover, $r_{tl} = 0.9$.

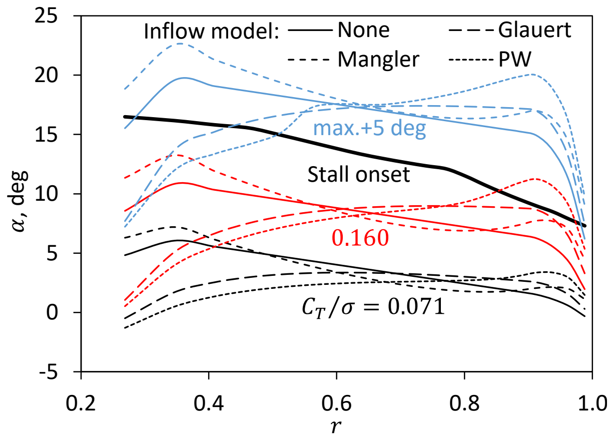

Figure 14: Radial distributions of angle of attack for various thrust levels and inflow models in hover, $r_{tl} = 0.9$.

At the tip region, the PW model shows the smallest inflow and thus, the largest angle of attack, while at the regions inboard of $r \approx 0.65$ it is vice versa. For the thrust level of $C_T/\sigma = 0.16$ the PW model is the only one that goes above the stall angle of attack near the tip region, while the Glauert and Mangler model remain below. This generates more airfoil and induced drag and therefore, because of the large distance to the hub center, more power required than the other inflow models.

Increasing the collective control by 5 deg above the maximum trimmable thrust (blue lines) the majority of radial stations is in post-stall conditions at very high angles of attack. Only the Glauert and PW inflow models are below stall inboard of $r \approx 0.45$, owing to the higher inflow ratio when compared to the Mangler model.

In Figure 16 the respective distributions of the section normal force, C_n, and moment about quarter chord, C_m, coefficients are plotted. The generally small angles of attack for $C_T/\sigma = 0.071$ are within the attached flow regime far away from stall all over the blade. This leads to moderate normal force and small negative moment coefficients (because of airfoil camber).

The high thrust $C_T/\sigma = 0.160$ comes along with higher normal force coefficients. The expected stall of the PW model in the outer region $0.85 < r < 1$ cannot immediately be seen in the normal force coefficient, because of the stall behavior at this Mach number is very gradual, see Figure 5 (b). However, the stall is seen in the moment coefficient of the PW model with the red dotted curve dropping sharply to larger negative values, Figure 16 (b). The other blade areas are close to stall, indicated by zero or slightly positive moment coefficients.

The blue lines are for the case where the collective control is increased by 5 deg over the individual maximum thrust achieved by the different inflow models. Nearly all radial stations are then in deep stall condition. Although the normal force coefficients are at the same levels of as for the $C_T/\sigma = 0.160$ case, the moment coefficients indicate deep stall almost all over the blade by their large negative values.

This is because from $r \approx 0.65$ toward the tip, the Mach numbers are exceeding 0.4 and the stall characteristics of the normal force coefficient are flattening out, see Figure 4. For $r < 0.6$, however, the PW and None inflow models show a significant loss of normal force coefficient in Figure 16 (a) as expected from Figure 15 (a), while the Glauert and PW inflow models remain below stall, which results in large C_n. In this area the moment coefficients for these two inflow models are close to zero, which indicates angles of attack close to stall, but not beyond, Figure 16 (b).

The maximum trimmable thrust:

As shown in Figure 10 and Figure 12 (a), the maximum trimmable thrust varies depending on the inflow model, the tip loss model, and the CF model. In the following, $r_{tl} = 0.9$ is used. Radial distributions of the inflow, angle of attack including stall onset, normal force and moment coefficients at the individual maximum trimmable thrust are shown. As before, the inflow models are identified by the line styles, and black curves are without the CF model, while including it the curves are red. In general, the inclusion of the CF model allows for higher maximum thrust for all inflow models, see Figure 12 (a).

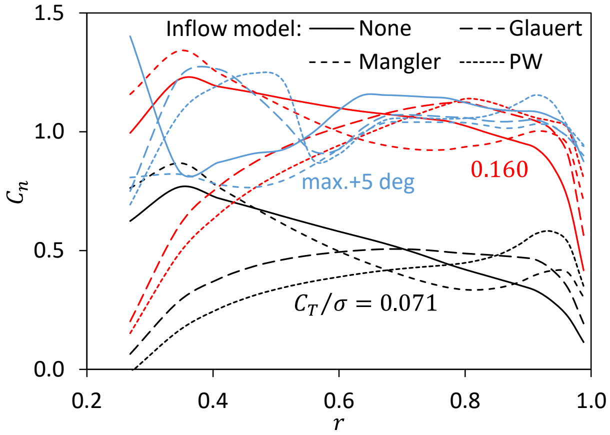

(a) normal force coefficient

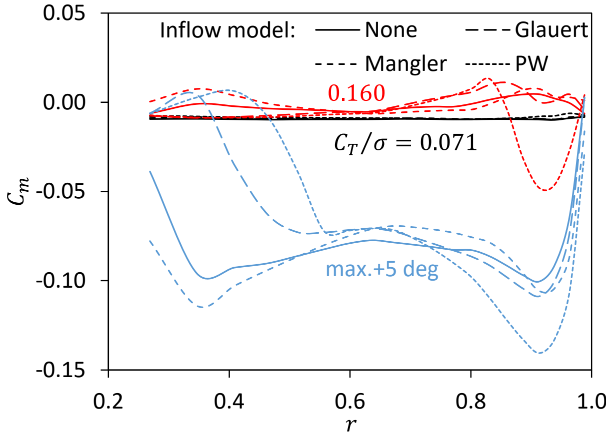

(b) moment coefficient

Figure 16: Radial distributions of aerodynamic coefficients for various thrust levels and inflow models in hover, $r_{tl} = 0.9$.

The inflow distributions are shown in Figure 17 and are rather comparable to the curves for $C_T/\sigma = 0.160$ in Figure 13, but at a higher value due to a higher thrust. Recall that each of the curves is for a different thrust, therefore the mean of the inflow models is differing as well. Due to the higher thrust with the CF model involved, the red curves are slightly higher than the black ones.

The distribution of angles of attack along span are given in Figure 18, which can be compared with the curves for $C_T/\sigma = 0.160$ of Figure 14, but here for the higher maximum trimmable thrust. Independent of the

CF model, all inflow models exceed the stall angle near the tip region.

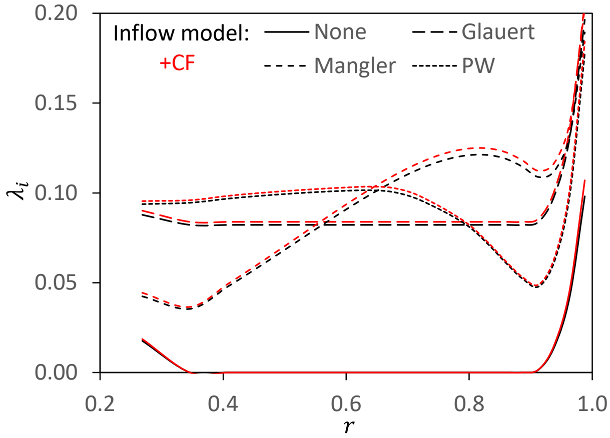

Figure 17: Radial distributions of the inflow ratio for maximum trimmable thrust and different inflow models in hover, $r_{tl} = 0.9$.

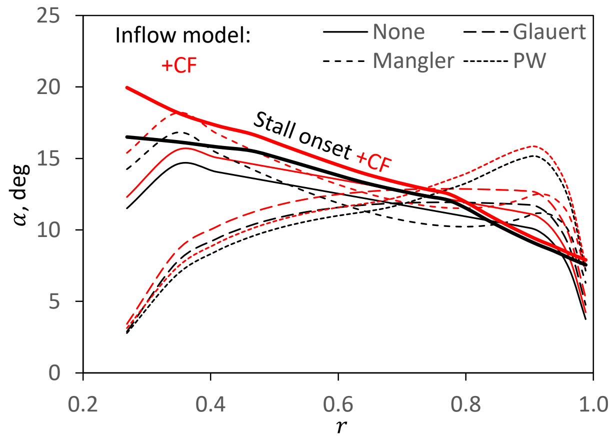

Figure 18: Radial distributions of angle of attack for maximum trimmable thrust and different inflow models in hover, $r_{tl} = 0.9$.

Most prominent is here the PW model, which is the only one that includes the tip vortex upwash due to the wake contraction, and thus increases the angle of attack there. In the region $0.75 < r < 0.95$ the angle of attack exceeds the stall angle. Inboard of it, the Glauert and PW models generate angles of attack significantly lower than the Mangler and None inflow models. Therefore, with the Mangler inflow model at $r \approx 0.35$ the stall angle is slightly exceeded, and the None inflow model remains below it.

The normal force and moment coefficient distributions then show the stall effects, see Figure 19, which can be compared to Figure 16 for the lower thrust of $C_T/\sigma = 0.160$. Because both the None and Mangler inflow models lead to angles of attack rather close to stall all over the radius (see Figure 18), their C_n values are close to the maximum normal force coefficients at each of the radial positions and their respective Mach numbers.

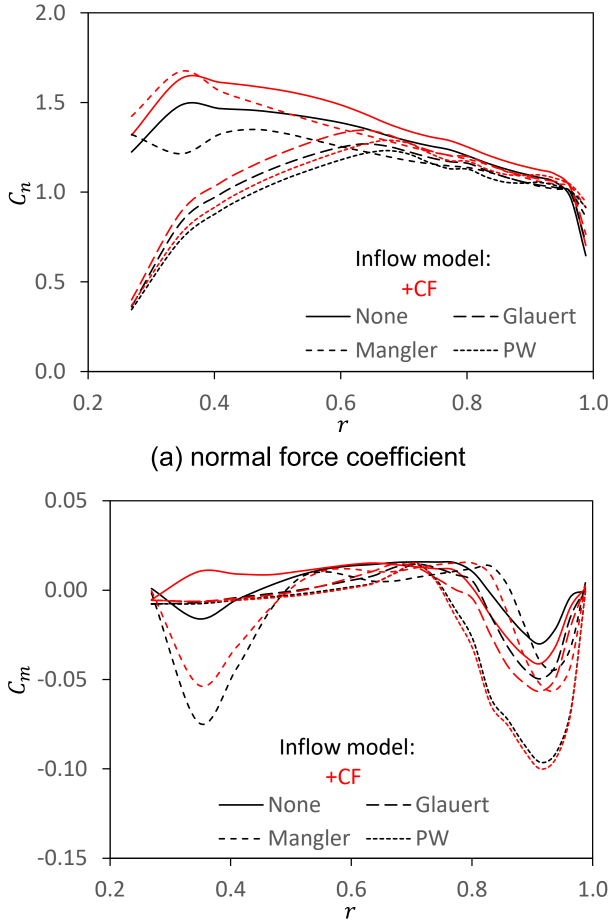

(a) normal force coefficient

(b) moment coefficient

Figure 19: Radial distributions of aerodynamic coefficients for various thrust levels and inflow models in hover, $r_{tl} = 0.9$.

In the region near the tip for $r > 0.75$ all inflow models generate rather similar C_n values, despite very different angles of attack. This is due to the flat $C_n(\alpha)$ curves at the higher subsonic Mach numbers experienced there, see Figure 5 (b).

Near $r \approx 0.35$ the Mangler model leads to slight stall without the CF model (black curve, see Figure 18), and due to the small Mach number there, see Figure 5 (a), the post-stall region is accompanied by a moderate drop in normal force coefficient, which is seen at that position in Figure 19 (a). When including the CF model, the angle of attack there just reaches the stall angle and the normal force coefficient reaches highest values.

Finally, the moment coefficient for these conditions of maximum trimmable thrust are shown in Figure 19 (b). The moment coefficient is much more sensitive to stall than the normal force coefficient, because in attached flow it remains at small negative values, but during stall sharply drops to larger negative values. This is seen especially at the tip region for all inflow models, and also near the root of the blade for the Mangler inflow model.

Concluding the hover investigations, the maximum trimmable thrust of the rotor always includes stall over some radial extent of the blade, at least for this rotor blade geometry. Therefore, to further enhance the thrust capability, the blade design must be changed in terms of twist distribution, chord distribution and airfoil selection, but that is out of the scope of this paper.

4.2. Forward flight: maximum trimmable thrust

In forward flight, here confined to a high advance ratio of $\mu = 0.4$, the shaft angle is prescribed to $\alpha_S = 0$ deg for reasons of simplicity and the trim procedure is applied as described before. Because of the lateral asymmetry of the flow, the trim now requires the collective and both cyclic control angles. At maximum trimmable thrust of the rotor the aerodynamic limit is reached. Higher thrust values are possible due to the high dynamic pressure on the advancing side, but the aerodynamic moments about the hub cannot be balanced any more by cyclic control angles, due to the low dynamic pressure on the retreating side.

Aerodynamic environment:

In this edgewise operating condition the velocity at the blade element becomes periodic. The tangential velocities, expressed by the Mach number component acting in chordwise direction, Mx, are shown in Figure 20. The free-stream is coming from the left and the sense of rotation is counter-clockwise. The rotor is seen from above, thus the advancing blade is on the top and the retreating blade at the bottom. This operational condition results in maximum Mach numbers of almost 0.9 at the tip of the advancing blade, while the tip of the retreating blade only experiences a Mach number of less than 0.4.

There, at an azimuth of $\psi = 270$ deg, the Mach number becomes zero at $r = \mu = 0.4$. Further inboard reversed flow conditions are acting on the blade with Mach numbers a little bit larger than 0.1. Zero tangential Mach number at a blade section is obtained along a circle with a radius of $\mu/2 = 0.2$ about the point $r = \mu/2, \psi = 270$ deg. The Mach number normal to the rotor blade (here only from thrust-induced inflow; in general also including inflow from rotor tilt, blade flapping motion, fuselage-induced velocities, etc.), usually is non-zero everywhere. Therefore, the actual angle of attack along the circle of $M_x = 0$ is $\alpha = \pm 90$ deg, depending on the direction of the resulting normal velocity component.

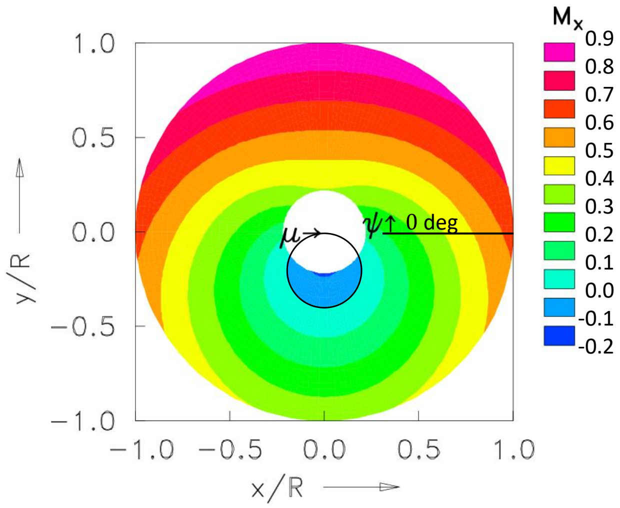

Figure 20: Mach numbers acting on the rotor blade for $\mu = 0.4,\ \alpha_S = 0$ deg.

Blade section forces are based on the dynamic pressure, i.e. essentially to the square of the Mach number distribution, which exaggerates the asymmetry of the flow between advancing and retreating side. This increases the level of lifting capability of the advancing blade tip and simultaneously decreases it on the retreating side, despite higher maximum lift coefficients at small Mach numbers and smaller ones at high Mach numbers.

Owing to the superposition of the blade's own circumferential speed and the free-stream velocity, yaw angles develop that reach up to ± 90 deg where $Mx = 0$, i.e. along the afore-mentioned circle on the retreating side. The distribution of the resulting yaw angle is given in Figure 21. The yaw angle is zero where the blade's leading edge is perpendicular to the oncoming free-stream, i.e. at $\psi = 90$ deg and 270 deg azimuth only. It achieves values slightly more than $\beta = \pm 20$ deg at the blade tip and up to $\beta = \pm 90$ deg for radial stations $r < 0.4$ on the retreating side. Such large yaw angles significantly delay stall, because the boundary layer is radially transported away. In the front half of the rotor disk, the flow is oriented radially inboard and in the rear half it is radially outboard. In the end, it adds to the CF effect outlined in Section 3.2, which is always oriented outboard and superimposes on the yaw angle.

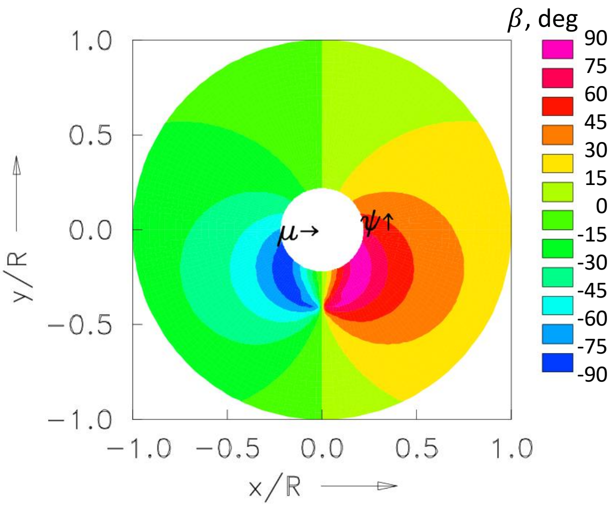

Figure 21: Yaw angles at the rotor blade for $\mu = 0.4$, $\alpha_S = 0$ deg.

Because of the wide range of Mach numbers encountered, the steady stall angle of attack also has a wider range than in hover, and is depending on both radial position and azimuth, see Figure 22. The iso-lines of the stall angles are naturally fitting to the Mach number distributions in Figure 20, and the radial distribution along $\psi = 0$ deg and 180 deg azimuth are the same as in hover, already shown in Figure 4.

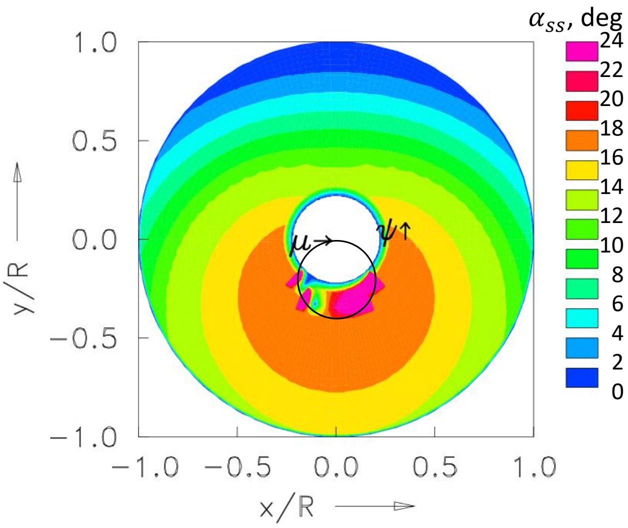

Figure 22: Steady stall angles (without CF and yaw model) at the rotor blade for $\mu = 0.4$, $\alpha_S = 0$ deg.

The stall delay caused by the combined yaw angle and CF models, and the contribution in stall delay from the unsteady aerodynamic model result in an effective stall angle of attack distribution as given in Figure 23 (a) for the nominal thrust with $C_T/\sigma = 0.071$ and in (b) for the maximum trimmable thrust with $C_T/\sigma = 0.126$. Further settings are: None inflow and $r_{tl} = 0.9$.

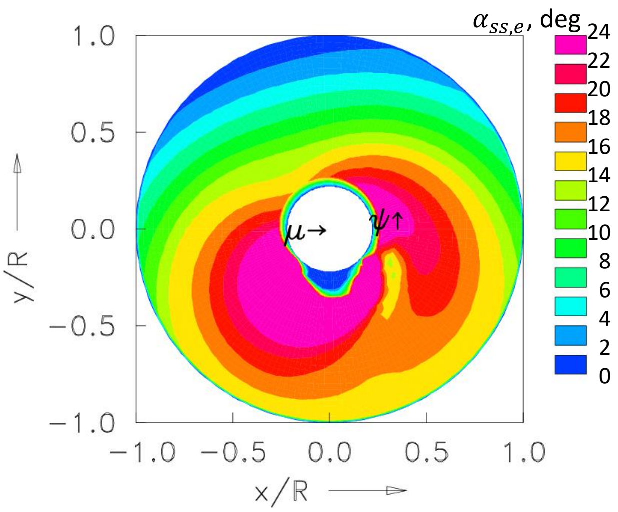

(a) nominal thrust, $C_T/\sigma = 0.071$

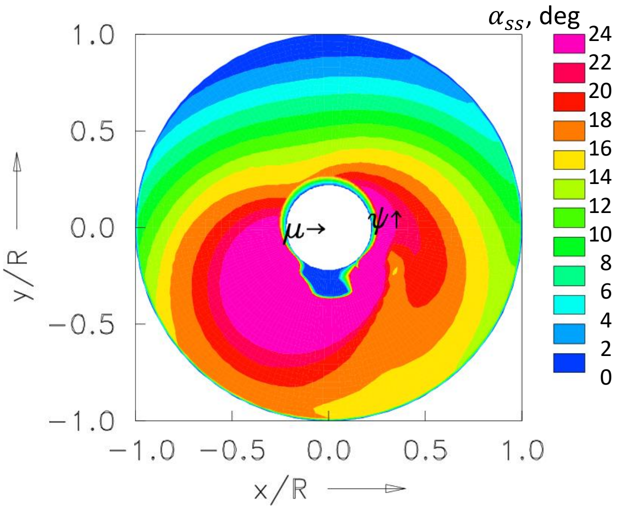

(b) maximum trimmable thrust, $C_T/\sigma = 0.126$

Figure 23: Effective instantaneous stall angles due to yaw angle, CF, and unsteady aerodynamics model at the rotor blade for $r_{tl} = 0.9$, $\mu = 0.4$, $\alpha_S = 0$ deg, None inflow.

Essentially the retreating side of the rotor profits from the stall delays. This leads to higher lift capability on the entire retreating side due to higher stall angles and the increase of lifting capability beyond that of steady unyawed aerodynamic modeling that comes with it. One contribution to the unsteady aerodynamics model is depending on the magnitude of the pitch rate of the blade. With a flexible blade, elastic torsion and blade flapping motion contribute as well, but here the blade is assumed as rigid only with pitching motion due to cyclic control angles. The pitch rate contribution is also depending on the thrust level, because the cyclic control angle amplitude increases with increasing thrust, and with it the pitch rate.

The stall angles in Figure 23 (a) for nominal thrust and the respective amplitude of the cyclic control angle are therefore smaller than those of the maximum trimmable thrust shown in (b). These results are for the None inflow model and tip loss setting of $r_{tl} = 0.9$.

The various inflow models at this high advance ratio now generate a radial and azimuthal variation, the magnitude depending on the thrust level. In contrast to the hovering condition, both the Glauert and Drees models now have a longitudinal gradient. While the Glauert model has no lateral gradient, it is $\lambda_{iS} = -2\mu\lambda_{i0}$ in the Drees model. This generates more downwash on the retreating side than on the advancing side, because for zero aerodynamic rolling moment the lift on the retreating side must be generated with a significantly smaller dynamic pressure than on the advancing side. Thus, the blade and tip vortex circulation on the retreating side must be stronger than on the advancing side, and the induced inflow of these as well.

The Mangler model has a non-linear radial distribution as in hover, but in forward flight also contains up to several harmonics (up to 6 are retained in S4), yet remains laterally symmetric (only cosine functions are involved). The PW model is entirely based on trailed vortices all along the span in the near wake. The far wake consists of root and tip vortices (and eventually a dual tip vortex system, depending on the radial lift distribution). All these trailed vortices are fed by the radially and azimuthally varying blade circulation, which results in a nonlinear radial and azimuthal inflow distribution with very high harmonic content, especially when blade-vortex interaction (BVI) occurs. Because the rotor shaft angle is set to $\alpha_S = 0$ deg, the rotor wake remains close to the rotor disk and BVI must be expected.

For a qualitative comparison amongst the models, the highest common thrust level of $C_T/\sigma = 0.115$ for the combination of unsteady aerodynamics with both yaw and CF models enabled, and the tip loss beginning at $r_{tl} = 0.9$, is chosen. First, the mean value of induced inflow at each blade element is extracted for each of the inflow models and shown in Figure 24. The data of Glauert's and Drees' inflow model are identical, since the longitudinal and lateral gradients do not affect the mean value.

The Mangler model exhibits a similar variation along span as in hover, but the PW model now shows a mean inflow higher than the other models near the tip region, and less inboard, while the None inflow model is zero. All inflow models are affected by the tip loss model with progressively increasing inflow towards the tip (and root), bringing the lift at the tip (and root) to zero. These distributions are essentially comparable to those of hover given in Figure 13, but at a significantly lower level because of the high advance ratio.

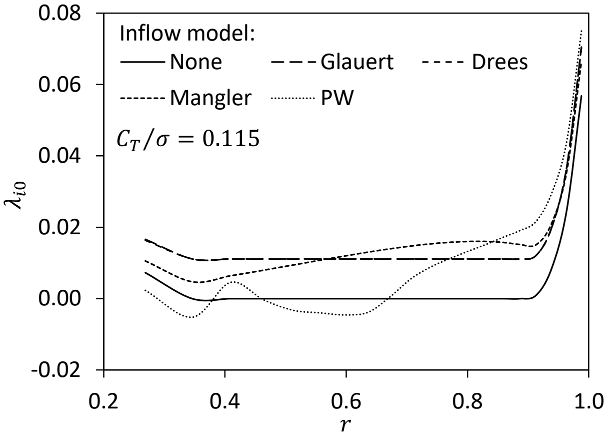

Figure 24: Mean inflow ratio distribution, $r_{tl} = 0.9$, $\mu = 0.4$, $\alpha_S = 0$ deg. Glauert and Drees data are identical.

More interesting, however, is the dynamic inflow content and the nonlinearity of its radial distribution. This can again best be represented by contour plots of the high-pass filtered inflow distribution, i.e. with the mean of Figure 24 removed.

First, the Glauert and Drees inflow models are compared, as they are in a similar range of dynamic cyclic magnitude, Figure 25. Clearly visible is the pure longitudinal variation of the Glauert model in Figure 25 (a), while the Drees model in (b) includes a lateral gradient of almost the same amount $\lambda_{iS} = -0.8 \approx -\lambda_{iC}$; therefore, the distribution appears rotated by 45 deg and magnified. The longitudinal gradient, however, is the same for both models, visible along the line $y/R = 0$.

In contrast to these, the Mangler and PW inflow models are highly nonlinear and with different higher harmonic content of inflow, shown in Figure 26 (a) and (b), respectively.

There is some comparability especially in the first harmonic content, because the Mangler model has a lateral symmetry with essentially a front-to-aft gradient, while the PW model shows the maximum inflow in the fourth quadrant and is in this regard more similar to the Drees model.

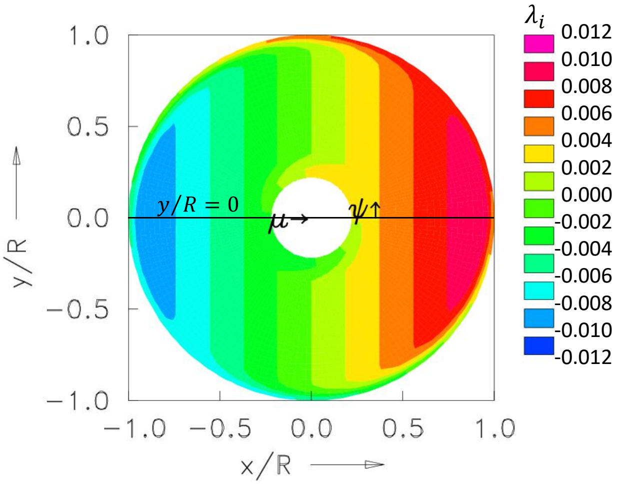

(a) Glauert model

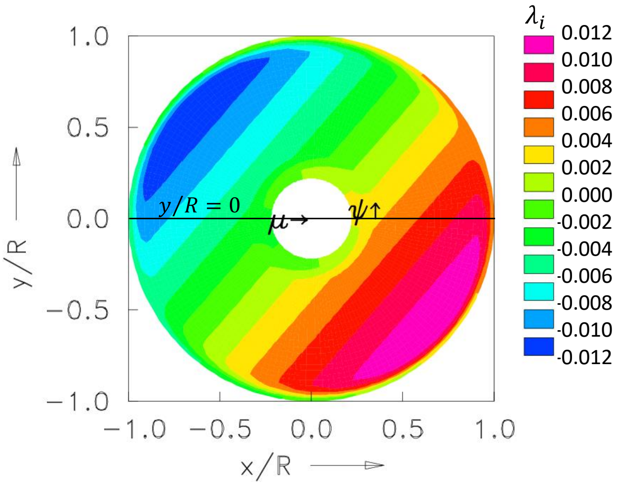

(b) Drees model

Figure 25: Dynamic content of the Glauert and Drees inflow models, $r_{tl} = 0.9,\ \mu = 0.4,\ \alpha_S = 0$ deg, $C_T/\sigma = 0.115$.

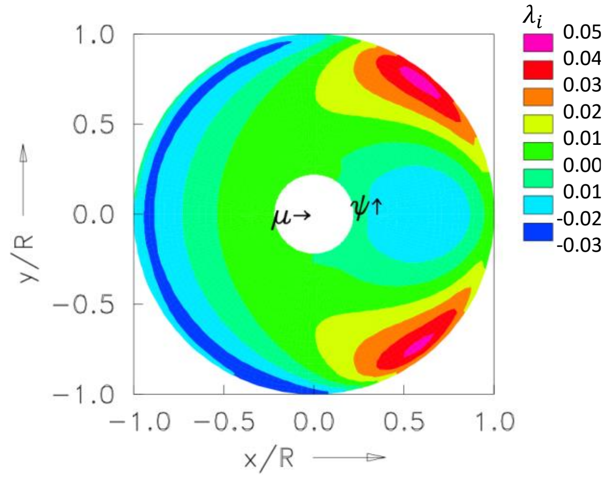

(a) Mangler model

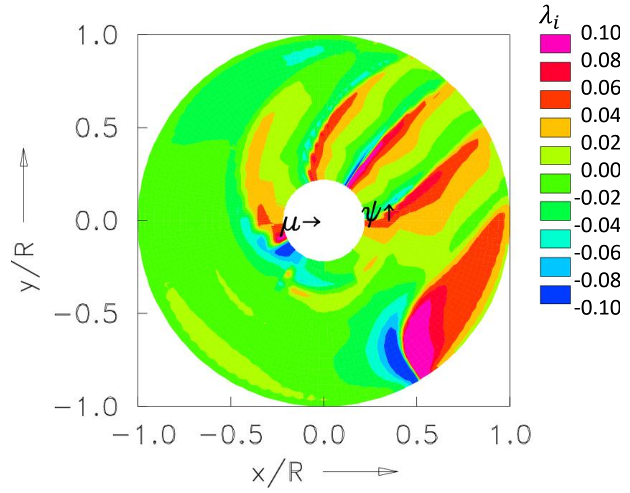

(b) PW model

Figure 26: Dynamic content of the Mangler and PW inflow models, $r_{tl} = 0.9,\ \mu = 0.4,\ \alpha_S = 0$ deg, $C_T/\sigma = 0.115$.

However, the Mangler model, Figure 26 (a), shows a strong concentration of maximum inflow at the blade tip around $\psi = 45$ deg and 315 deg azimuth, introducing some higher harmonic content to the airloads. The PW model, because it is based on trailed vortices of small core radius (significantly less than the chord length of the blade), reveals a sequence of BVI on the advancing side and one on the retreating side, Figure 26 (b).

Note that the color scaling is different for the Mangler and PW inflow models; the peak values at the vortex core radius experienced during BVI partly still exceed the color range by a factor of two. One strong BVI event is found on the retreating side around $\psi = 315$ deg, while the range 180 deg $\leq \psi \leq 300$ deg is found with relative constant inflow. All along the front of the rotor disk an upwash is predicted.

These different inflow models will have impact on the maximum trimmable rotor thrust at this advance ratio (especially when the rotor blades are elastic and respond to these aerodynamic excitations, which is out of the scope of this paper).

At maximum thrust, stall is expected to develop somewhere in the third quadrant. All of the inflow models have a smooth distribution of inflow there. Even the PW model in Figure 26 (b) suggests the possibility of vortex-induced stall only in the fourth quadrant around an azimuth of $\psi \approx 300$ deg near the blade tip, but not before. There, the approaching blade first experiences a sharp increase of upwash (blue) that might trigger a stall event, followed shortly after by an equally strong downwash.

Maximum trimmable thrust:

Due to the large possible amount of combinations of inflow models with steady or unsteady aerodynamics, without or with yaw and CF models, without or with the VS model, and the various tip loss settings (all of them were computed during this study), only a very small subset of results can be shown here.

The results for thrust and power of the various inflow models are combined in graphs of the same computational setup, identified by a configuration acronym as given in Table 3. From all possible combinations, only a subset is used here that best reflect the changes from most simple (sAnynVS = steady Aerodynamics, no CF+yaw, no VS) to most advanced modeling (uAwywVS = unsteady Aerodynamics, with CF+yaw, with VS).

Table 3: Configuration acronyms used.

Acronym	Aerodynamics	CF+yaw	VS	level
sAnynVS	steady	no	no	lowest
uAnynVS	unsteady	no	no	
sAwynVS	steady	with	no	
uAwynVS	unsteady	with	no	
uAwywVS	unsteady	with	with	highest

Results for the power vs. thrust curve are shown in Figure 27 to first visualize the effect of steady (a) versus unsteady aerodynamics modeling (b) without CF, yaw and VS models. In (c) again steady aerodynamics are used, but now the yaw and CF models are active to isolate their impact on the results. The begin of tip loss was varied from $r_{tl} = 0.8$ (black curves) to 0.9 (red), and the various inflow models are identified by the different line styles.

In general, for the larger extent of tip loss, $r_{tl} = 0.8$, stall is earlier experienced and the maximum thrust is less than for $r_{tl} = 0.9$. For the same reason, the power required for a given thrust is also always higher for $r_{tl} = 0.8$ than for $r_{tl} = 0.9$. With unsteady aerodynamics modeling, shown in Figure 27 (b), a stall delay during the increase of angle of attack on the retreating side is generated. This results in higher possible lift capability and thus higher maximum thrust capability, associated with less power required than for the steady aerodynamics cases shown in Figure 27 (a). From the variety of inflow models, the lowest maximum thrust is obtained with the PW model, which is not surprising considering its high dynamic content of inflow with also much larger local peak values than any other inflow model.

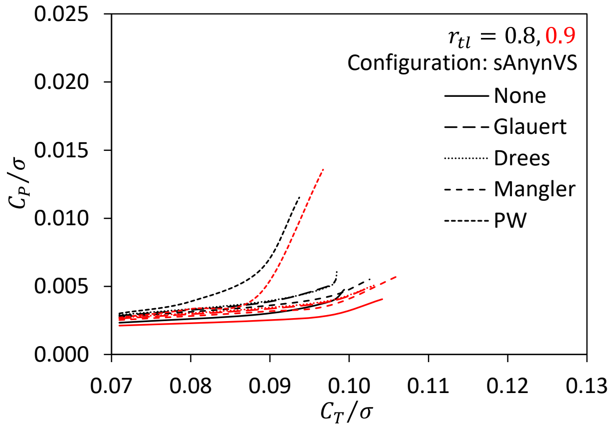

(a) steady Aerodynamics, no CF+yaw, no VS

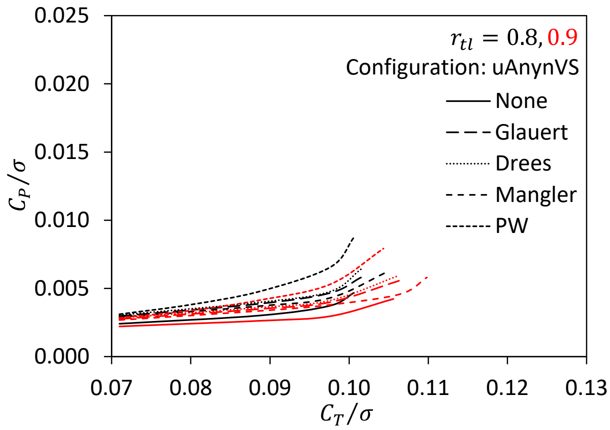

(b) unsteady Aerodynamics, no CF+yaw, no VS

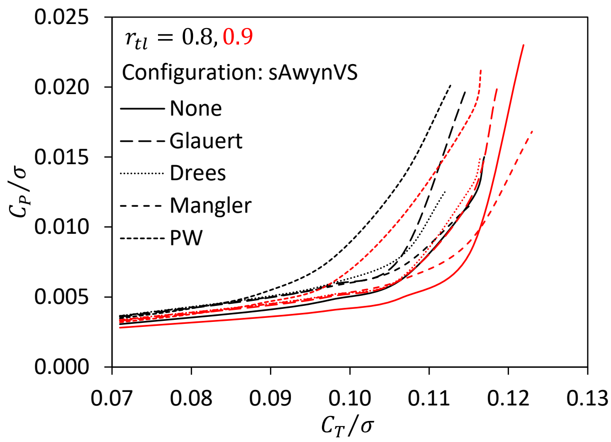

(c) steady Aerodynamics, with CF+yaw, no VS

Figure 27: Power vs. thrust curves for various inflow models and tip loss settings, showing the effect of steady versus unsteady aerodynamics and versus CF+yaw modeling, $\mu = 0.4$, $\alpha_S = 0$ deg.

The Glauert and Drees model results are almost line on line, because Drees' lateral gradient is compensated by an equivalent amount of cyclic control angle Θ_S, and hence the lateral inflow gradient does not play a role here.

The effect of the CF+yaw models is shown in Figure 27 (c), combined with steady aerodynamics. As can be seen, the increase in maximum possible thrust relative to Figure 27 (a) is much larger than the one due to unsteady aerodynamic modeling shown in (b). Now the stall delay is not caused by the rate of angle of attack, rather by the combined CF and yaw effect. The resulting increase in stall angle was shown in Figure 23. Because these stall delays are much larger than those obtained by the unsteady aerodynamics model, the maximum trimmable rotor thrust is also much larger. The impact of the different inflow models is the same as before.

Next, both unsteady aerodynamics and the CF+ yaw models are combined in Figure 28 (a) and finally the VS model is added in (b). As expected, the combined unsteady aerodynamics and yaw effects result in a further delay of airfoil stall and therefore in a higher maximum trimmable thrust, compared to the individual models' results shown before in Figure 27 (b) and (c). The maximum trimmable thrust is obtained around $C_T/\sigma = 0.125$ for $r_{tl} = 0.9$ with the Mangler, PW and None inflow models. The Glauert model reaches 0.122 and the Drees model 0.119. Compared to the steady aerodynamics without CF+yaw models in Figure 27 (a), the maximum thrust values range between $C_T/\sigma = 0.095$ (PW) to 0.105 (Mangler). Therefore, the stall delay caused by unsteady aerodynamics, CF and yaw result in a significant improvement of maximum trimmable thrust.

Some example time histories of airfoil coefficients for increasing thrust at a radial station of $r = 0.637$ (chosen because significant stall effects are expected around this radial position on the retreating side) are shown next to give an insight into the physics computed by the various models. First, the Glauert model results for normal force and moment coefficient time histories are shown in Figure 29 (a) and (b) for the simplest (sAnynVS) and the most advanced configuration (uAwywVS) in Figure 30 (a) and (b).

Because the inflow distribution of this model is very smooth, see Figure 25 (a), the variation of angle of attack is smooth as well and the time history of the normal force coefficient in Figure 29 (a) is essentially sinusoidal for small thrust. The highest trimmable thrust for this simple configuration is rather low and stall develops on the retreating side with an associated pitching moment dip as seen in Figure 29 (b).

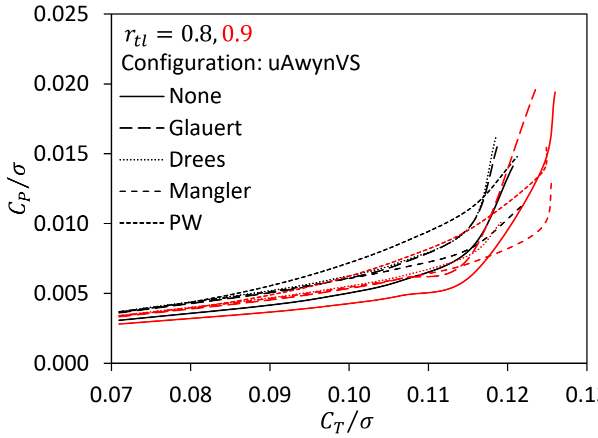

(a) unsteady Aerodynamics, with CF+yaw, no VS

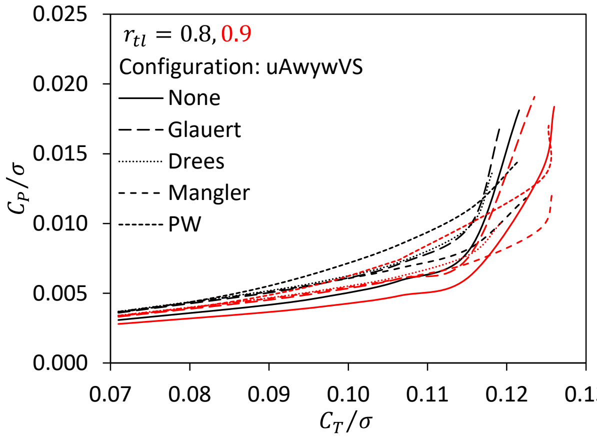

(b) unsteady Aerodynamics, with CF+yaw, with VS

Figure 28: Power vs. thrust curves for various inflow models and tip loss settings, showing the effect of combined unsteady aerodynamics and CF+yaw modeling versus further adding the VS model, $\mu = 0.4$, $\alpha_S = 0$ deg.

The most complex configuration (uAwywVS) in Figure 30 (a) shows much higher lifting capability on the retreating side due to significant stall delay of the unsteady, CF and yaw models. VS appears after stall onset in both normal force and moment coefficients, Figure 30 (b). Large negative C_m values are obtained, indicating deep stall.

Results for the same configurations, but now using the Mangler inflow model, are given in Figure 31, whose inflow distribution was shown in Figure 26 (a). The higher harmonic content of this inflow model also leads to some higher harmonic variations in the normal force coefficient, Figure 31 (a). As for the Glauert model, the maximum trimmable thrust is limited by the small lift coefficients achievable on the retreating side. Stall onset is indicated there, but the moment coefficient in Figure 31 (b) shows only moderate stall.

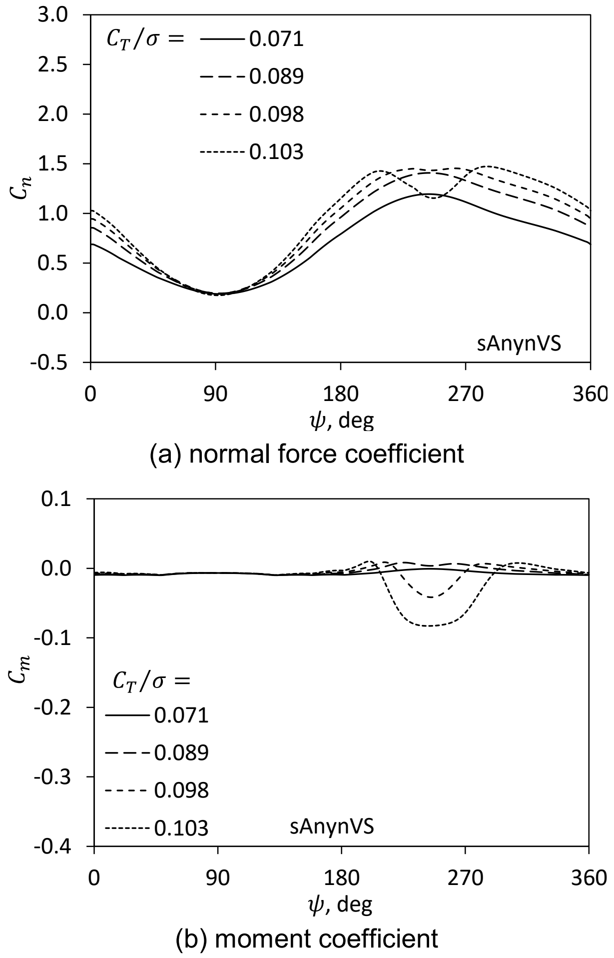

(a) normal force coefficient

(b) moment coefficient

Figure 29: Aerodynamic coefficients at $r = 0.637, \mu = 0.4$ for different thrust levels, Glauert inflow model, $r_{tl} = 0.9$. Most simple configuration settings.

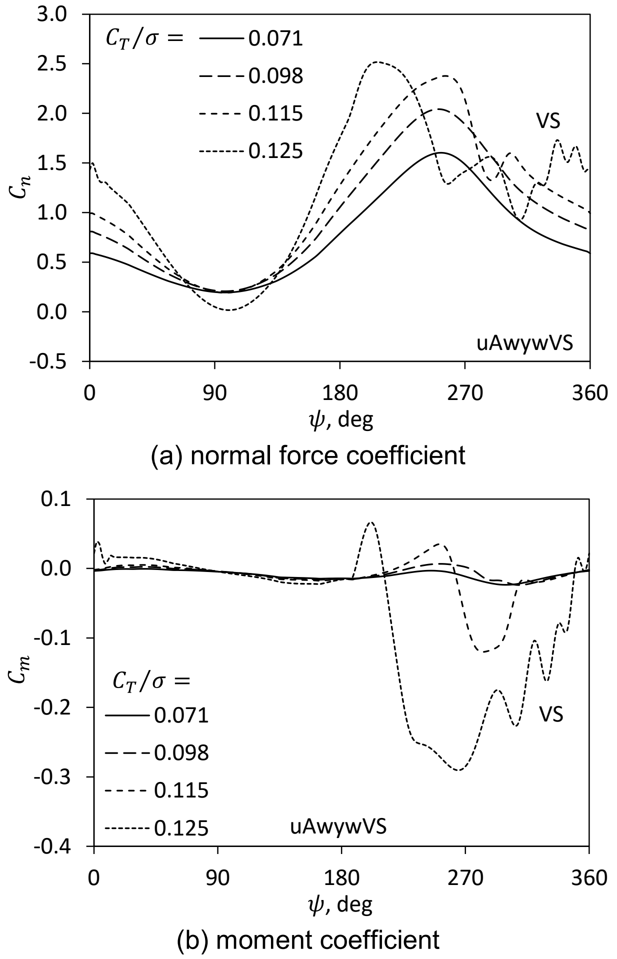

(a) normal force coefficient

(b) moment coefficient

Figure 30: Aerodynamic coefficients at $r = 0.637, \mu = 0.4$ for different thrust levels, Glauert inflow model, $r_{tl} = 0.9$. Most advanced configuration settings.

Results for the most advanced setting (uAwywVS) are given in Figure 32 (a) for the normal force and in (b) for the moment coefficients with deep stall events in both. Again, the effect of stall delay caused by unsteady aerodynamics, CF and yaw allow for significantly higher lift on the retreating side, and this results in significantly higher trimmable rotor thrust. This is possible because other areas on the retreating side remain unstalled and provide the required lift for trimming to zero aerodynamic hub moments.

With increasing thrust the cyclic control angles also increase, and with them the pitch rate. The higher the pitch rate, the larger the stall delay of the unsteady aerodynamic model. This adds additional stall delays to the CF and yaw models.

Last, the PW inflow model results are shown in Figure 33 for the simplest configuration (sAnynVS) and in Figure 34 for the most advanced setting (uAwywVS).

Now BVI is included on both the advancing and the retreating sides, see Figure 26 (b). Using steady aerodynamics, the BVI generates large variations in the angle of attack, and thus in the normal force coefficient in Figure 33 (a), but limited to a very small azimuthal region around the vortex core. Stall is sometimes better seen in the aerodynamic moment, and from Figure 33 (b) it can be judged that on the advancing side no stall events take place, just a few wiggles of moderate magnitude can be seen in the moment.

This is different on the retreating side. Although the normal force coefficient does not exhibit larger variations than the BVI on the advancing side, here the moment clearly indicates stall onset even for the lowest thrust level. With increasing thrust, the stalled region grows accordingly with moment values becoming highly negative, which indicates deep stall.

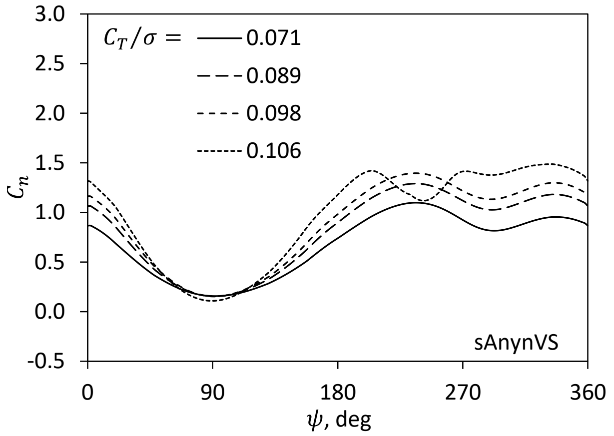

(a) normal force coefficient

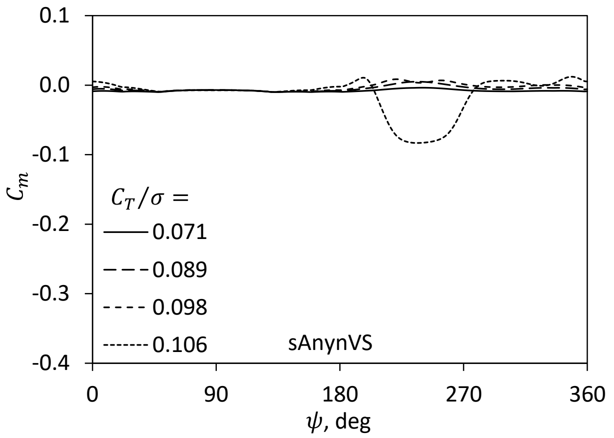

(b) moment coefficient

Figure 31: Aerodynamic coefficients at $r = 0.637, \mu = 0.4$ for different thrust levels, Mangler inflow model, $r_{tl} = 0.9$. Most simple configuration settings.

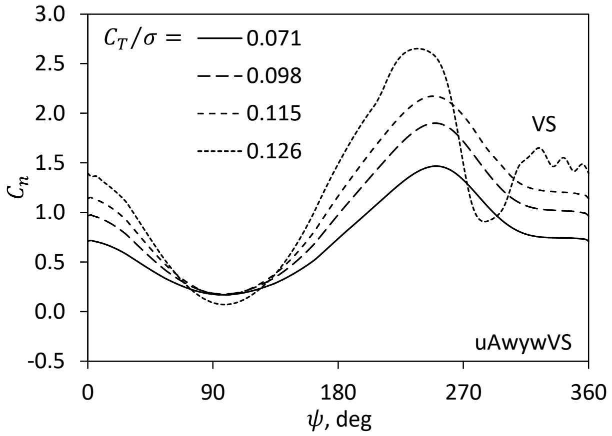

(a) normal force coefficient

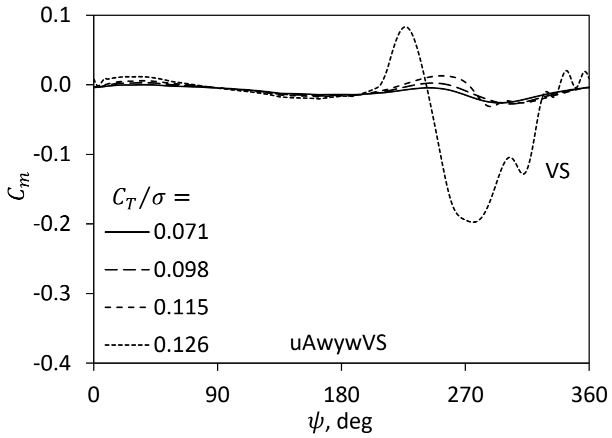

(b) moment coefficient

Figure 32: Aerodynamic coefficients at $r = 0.637, \mu = 0.4$ for different thrust levels, Mangler inflow model, $r_{tl} = 0.9$. Most advanced configuration settings.

The most advanced settings, Figure 34 (a) and (b), employ the unsteady aerodynamics model not only for the pitching motion, but also for the BVI, which is a gust problem with a different lift transfer function. For these high reduced frequencies of BVI events the effective angle of attack variation is drastically reduced relative to the geometric angle of attack. This leads to significantly smaller BVI-related lift fluctuations, as seen now in the normal force coefficient on the advancing side, compare Figure 34 (a) with Figure 33 (a).

Also, the vortex-induced stall seen in the steady aerodynamics even for the lowest thrust level, Figure 33 (b), practically disappears now in Figure 34 (b) due to the unsteady aerodynamics model. As for the former inflow models, the general effect of unsteady aerodynamic, CF and yaw models all engaged leads to much higher lift capability on the retreating side due to significant stall delays.

The maximum trimmable thrust becomes much higher than without these refinements in modeling, and despite deep stall over wide ranges at this radial station the rotor still can be trimmed.

The results now show major events expected in reality: BVI, stall delay, deep stall, and VS in the post-stall region until re-attachment takes place. Although all models employed are semi-empirical, they appear to represent the physics in an appropriate manner.

5. CONCLUSIONS

Hovering condition:

1. Both the constant inflow (Glauert) and prescribed wake (PW) models have larger inflow ratio in the inner parts of the rotor and less in the outer region than the Mangler model. This leads to smaller angles of attack in the inner regions and larger ones at the blade tip, compared to the Mangler model.

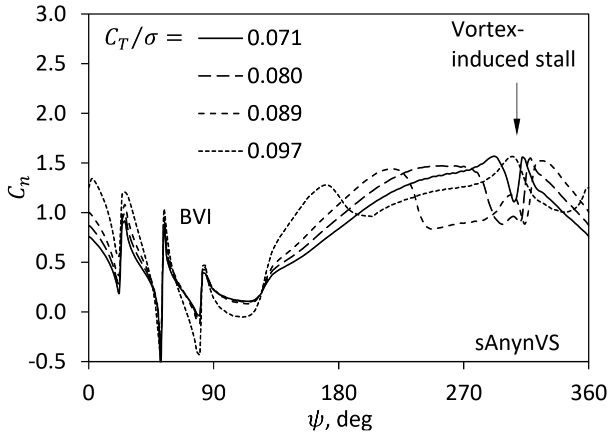

(a) normal force coefficient

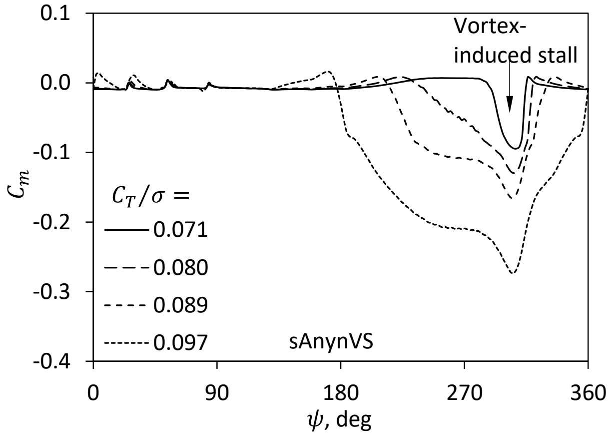

(b) moment coefficient

Figure 33: Aerodynamic coefficients at $r = 0.637, \mu = 0.4$ for different thrust levels, PW inflow model, $r_{tl} = 0.9$. Most advanced configuration settings.

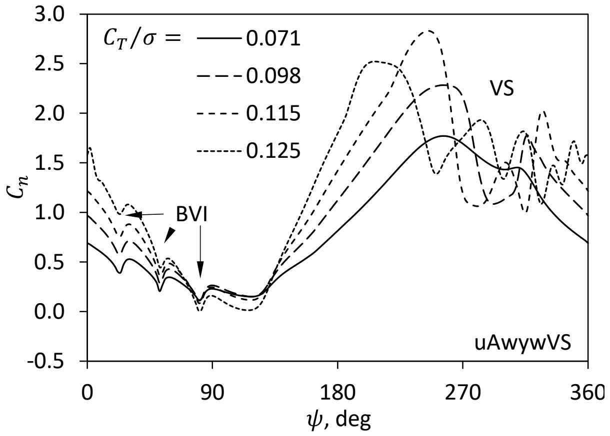

(c) normal force coefficient

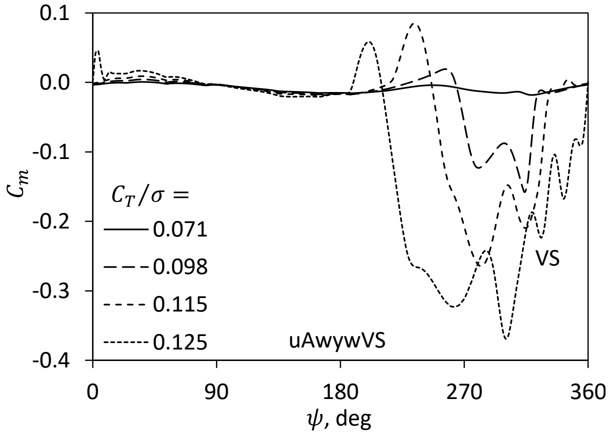

(d) moment coefficient

Figure 34: Aerodynamic coefficients at $r = 0.637, \mu = 0.4$ for different thrust levels, PW inflow model, $r_{tl} = 0.9$. Most advanced configuration settings.

2. The highest possible thrust is predicted by the Mangler model, because of its high inflow in the outer region of the blade with small stall angles.

3. Increasing the tip loss region reduces the maximum possible thrust due to increased loss of lift in the tip region. Reasonable values for high thrust range from $r_{tl} = 0.8 - 0.9$.

4. The centrifugal force (CF) model delays steady stall from small values at the blade tip progressively to larger values at the blade root. This has a significant impact on increasing the maximum thrust prediction.

5. The maximum figure of merit (FM) is found in the range of $C_T/\sigma = 0.1$ to 0.12, significantly below the maximum possible thrust. The larger the tip loss, the smaller the FM. Up to the maximum FM the CF model has virtually no impact on the results, because max. FM is obtained in attached flow conditions.

Forward flight:

1. The Glauert and Drees inflow models keep the flow environment at the blade smooth with moderate longitudinal and lateral gradients, but without higher harmonic content. Results for these are very similar. Stall occurs due to large angles of attack on the retreating side and limits the maximum trimmable thrust. Similar is true for the Mangler model, with some higher harmonic content added.

2. The prescribed wake (PW) inflow model introduces blade-vortex interaction (BVI) with locally large induced velocities. Steady aerodynamics over-estimate the lift response due to BVI and thus generate vortex-induced stall.

3. Yaw modeling significantly delays stall onset, further delays stem from CF effects and the unsteady aerodynamics. This allows for significantly

higher maximum trimmable thrust, despite deep stall developing.

4. BVI events require unsteady aerodynamic modelling of the gust problem. This brings down the large lift response of steady aerodynamics to realistic values observed in measurements and partly eliminates vortex-induced stall that is present in steady aerodynamics.

5. All the models employed are of semi-empirical, yet physical nature. Their parameters may be modified in a physical meaningful range to match measured data of rotors with maximum trimmable thrust, or in the vicinity of these.

Author contact:

Berend G. van der Wall, berend.vanderwall@dlr.de

6. ACKNOWLEDGMENTS

This study is funded within the DLR project URBAN-Rescue to develop best practices in use of comprehensive rotor codes and to identify their limits in application.

7. REFERENCES

JAHS = Journal of the American Helicopter Society

1. Bailey, F.J. Jr., and Gustafson, F.B., “Observations in flight of the region of stalled flow over the blades of an autogiro rotor,” NACA TN 741, 1939.

2. Gustafson, F.B., and Myers, G.C. Jr., “Stalling of Helicopter Blades (Contributions to the Aerodynamics of Rotary-Wing Aircraft),” NACA TR 840, pp. 105-110, 1946.

3. Sissingh, G., “Beitrag zur Aerodynamik der Drehflügelflugzeuge,” TH Hannover, Dissertation D89, 1940.

4. Focke, H., “Fortschritte des Hubschraubers,” Vortrag gehalten auf der 7. Wissenschafts-sitzung der Ordentlichen Mitglieder am 1. Oktober 1943, Sitzungsperiode 1943/44, Schriften der Deutschen Akademie der Luftfahrtforschung, no. 1070/43g, 1943.

5. Betz, A., (Ed.), “Monographien über Fortschritte der deutschen Luftfahrtforschung (seit 1939). N Überblick über die deutsche Entwicklung und Forschung auf dem Gebiete der Drehflügelflugzeuge,” compiled by G.J. Sissingh, AVA Göttingen, Germany, 1946. Translation in: van der Wall, B.G. (Ed.), *Göttinger Monograph N: German Research and Development on Rotary-Wing Aircraft, (1939 to 1945),* AIAA Library of Flight, Reston, VA, 2015.

6. Bellinger, E.D., “Analytical Investigation of the Effects of Blade Flexibility, Unsteady Aerodynamics, and Variable Inflow on Helicopter Rotor Stall Characteristics,” JAHS, Vol. 17, no. 3, pp. 35-44, 1972.

7. Hardy, W.G.S., “The Effects of Reynolds Number on Rotor Stall,” Symposium on Status of Testing and Modeling Techniques for V/STOL Aircraft, Philadelphia, PA, 1972.

8. McCroskey, W.J., Fisher, R.K., Jr., “Detailed Aerodynamic Measurements on a Model Rotor in the Blade Stall Regime,” JAHS, Vol. 17, no. 1, pp. 20-30, 1972.

9. Landgrebe, A.J., Bellinger, E.D., „ A Systematic Study of Helicopter Rotor Stall using Model Rotors,” 30th Annual Forum of the American Helicopter Society, Washington, D.C., 1974.

10. Amer, K.B., LaForge, S.V., “Maximum Rotor Thrust Capabilities, Articulated and Teetering Rotors,” Technical Note, JAHS, Vol. 22, no. 1, pp. 11-12, 1977.

11. McHugh, F.J., “What are the Lift and Propulsive Force Limits at High Speed for the Conventional Rotor?” 34th Annual Forum of the American Helicopter Society, Washington, D.C., 1978.

12. Yeo, H., “Calculation of Rotor Performance and Loads Under Stalled Conditions,” Proceedings of the 59th Annual Forum and Technology Display, Phoenix, AZ, 2003.

13. Johnson, W., “Technology Drivers in the Development of CAMRAD II,” American Helicopter Society Aeromechanics Specialist Meeting, San Francisco, CA, 1994.

14. Johnson, W., *Rotorcraft Aeromechanics*, Cambridge University Press, New York, 2013, Chapter 12.

15. Petot, D., Arnaud, G., Harrison, R., Stevens, J., Dieterich, O., van der Wall, B.G., Young, C., and Széchényi, E., “Stall Effects and Blade Torsion - An Evaluation of Predictive Tools,” JAHS, Vol. 44, no. 4, pp. 320-332, 1999.

16. Betz, A., “Schraubenpropeller mit geringstem Energieverlust (Propeller with Minimum Energy

Loss),” with an addendum from L. Prandtl, Göttinger Nachrichten, p. 193, 1919.

17. van der Wall, B.G., Lim, J.W., Smith, M., Jung, S.N., Bailly, J., Baeder, J.D., and Boyd, D.D., “The HART II International Workshop: An Assessment of the State-of-the-Art in Comprehensive Code Prediction,” CEAS Aeronautical Journal, Vol. 4, no. 3, pp. 223-252, 2013.
18. Gormont, R. E., “A Mathematical Model of Unsteady Aerodynamics and Radial Flow for Application to Helicopter Rotors,” USAAVLABS TR 72-67, 1973.
19. Bielawa, R.L., “Synthesized Airfoil Data Method with Applications to Stall Flutter Calculations,” 31st Annual Forum of the American Helicopter Society, Washington, D.C.,1975.
20. Tran, C.T., Petot, D., "A Semi-Empirical Model for the Dynamic Stall of Airfoils in View of the Application to the Calculation of Responses of Helicopter Blade in Forward Flight," VERTICA, Vol. 5, no. 1, pp. 35-53, 1981.
21. Beddoes, T.S., “Practical Computation of Unsteady Lift,” VERTICA, Vol. 7, no. 2, pp. 183-197,1983.
22. Gangwani, S.T., "Synthesized Airfoil Data Method for Prediction of Dynamic Stall and Unsteady Airloads," VERTICA, Vol. 8, no. 2, pp. 93-118, 1984.
23. Leiss, U., “A Consistent Mathematical Model to Simulate Steady and Unsteady Rotor-Blade Aerodynamics,” 10th European Rotorcraft Forum, The Hague, Netherlands, 1984.
24. Leiss, U. “Unsteady Sweep – a Key to Simulation of Three-Dimensional Rotor Blade Airloads,” 11th European Rotorcraft Forum, London, UK, 1985.
25. Leishman, J.G., Beddoes, T.S., “A Semi-Empirical Model for Dynamic Stall,” JAHS, Vol. 23, no. 3, pp. 3-17, 1989
26. Petot, D., “Differential Equation Modeling of Dynamic Stall,” La Recherche Aerospatiale, 1989, no. 5 (corrections dated October 1990)
27. Truong, V.K., “A 2-D Dynamic Stall Model Based on a Hopf Bifurcation,” 19th European Rotorcraft Forum, Marseilles, France, 1998.
28. van der Wall, B.G.: “An Analytical Model of Unsteady Profile Aerodynamics and its Application to a Rotor Simulation Program,” 15th European Rotorcraft Forum, Amsterdam, Netherlands, 1989.
29. Theodorsen, T., “General Theory of Aerodynamic Instability and the Mechanism of Flutter, NACA Report 496, 1935.
30. Glauert, H., “A General Theory of the Autogyro,” ARC R&M 1111, 1926.
31. Meijer-Drees, J.M., “A Theory of Airflow Through Rotors and its Application to Some Helicopter Problems,” Journal of the Helicopter Association of Great Britain, Vol. 3, no. 2, 1949.
32. Wheatley, J.B., “An Aerodynamic Analysis of the Autogiro Rotor with a comparison between Calculated and Experimental Results,” NACA TR 487, 1934.
33. Sissingh, G.J., “Beitrag zur Aerodynamik der Drehflügelflugzeuge,” Luftfahrt-Forschung, Vol. 15, no. 6, pp. 290-302, 1938; Translation in: “Contributions to the Aerodynamics of Rotary-Wing Aircraft,” NACA TM 921, 1939.
34. Mangler, K.W., and Squire, H.B., “The Induced Velocity Field of a Rotor,” ARC R&M 2642, 1950.
35. Beddoes, T.S., “A Wake Model for High Resolution Airloads,” International Conference on Rotorcraft Basic Research, National Institute of Environmental Health Sciences Research, Triangle Park, NC, 1985.
36. van der Wall, B.G.: “The Effect of HHC on the Vortex Convection in the Wake of a Helicopter Rotor,” *Aerospace Science and Technology*, Vol. 4, no. 5, pp. 320-336, 2000.
37. van der Wall, B.G., Yin, J., “Semi-Empirical Modeling of Fuselage-Rotor Interference for Comprehensive Codes: Influence of Angle of Attack,” *CEAS Aeronautical Journal*, Vol. 6, no. 4, pp. 557-574, 2015.
38. Küfmann, P.M., Bartels, R., van der Wall, B.G., Schneider, O., Holthusen, H., and Postma, J., “The Second Wind-Tunnel Test of DLR’s Multiple Swashplate System - IBC on a five-bladed rotor with fuselage-mounted (fixed frame) actuators,” *CEAS Aeronautical Journal*, Vol. 10, no. 2, pp. 385-402, 2019.